International Journal of Applied Earth Observation and Geoinformation 149 (2026) 105276

Contents lists available at ScienceDirect

International Journal of Applied Earth Observation and Geoinformation

journal homepage: www.elsevier.com/locate/jag

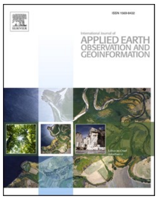

Annual and diurnal temperature cycle modelling of a merged multi-annual ECOSTRESS and Landsat land surface temperature dataset

Lluís Pérez-Planells [*], Frank-M. Göttsche [**], Jan Cermak

IMKASF, Karlsruhe Institute of Technology (KIT), Hermann-von-Helmholtz-Platz 1, 76344 Eggenstein-Leopoldshafen, Germany

ARTICLE INFO

Keywords:
Land surface temperature
Diurnal temperature cycle
Annual temperature cycle
ECOSTRESS
Landsat
LST modelling

ABSTRACT

Annual and diurnal temperature cycle (ATC and DTC) models are proven tools to estimate LST dynamics. Based on solar geometry, they typically require 3 to 6 parameters determined by fitting them to a LST dataset. The combined ADTC model employed here uses five controlling parameters to represent both cycles simultaneously, i.e., it allows to estimate the average annual and diurnal temperature cycle dynamics from five fitted parameters. High spatial resolution (70 m) model parameters were obtained for first time from a six year (2018 – 2023) datacube of merged ECOSTRESS and Landsat LSTs. Since LSTs at actual observation times were modelled, the variable overpass time of ECOSTRESS helped to sample the diurnal cycle. All available ECOSTRESS and Landsat LSTs over the four European cities Karlsruhe (Germany), Paris (France), Madrid (Spain) and Valencia (Spain) were obtained. The mean RMSE of the modelled LST over these study areas was 3.8 K. The high-resolution model parameters were compared against those obtained for MODIS for the same period and areas. The results showed RMSEs of 1.6 K, 2.0 K, 6.5 K, 0.2 h and 6.8 days for annual minimum temperature, annual amplitude, daily maximum amplitude, mean thermal noon and lag with respect to summer solstice, respectively. The larger RMSEs observed for maximum daily amplitude and lag with respect to summer solstice are attributed to insufficient data around thermal noon in the high-resolution dataset. The parameters were analyzed over rural and urban areas and show clear potential for more detailed urban thermal studies and land cover change monitoring.

1. Introduction

Annual and diurnal temperature cycle models reproduce the dynamic variation of the land surface temperature (LST) based on solar geometry (Göttsche and Olesen, 2009; Weng and Fu, 2014; Bechtel, 2015). In the last decades, the application of ATC and DTC models has gained popularity due to their capability to summarize LST variations with few parameters, typically 3 for ATC models and from 4 to 6 for DTC models. ATC and DTC models have been employed in different research topics, including Urban Heat Island (UHI) studies (Fu and Weng, 2018), LST disaggregation (Sismanidis et al., 2017), LST component separation (Liu et al., 2020), satellite orbital drift correction (Ma et al., 2020), under-cloud LST retrieval (Yang et al., 2024) and spatial representativity analysis of ground validation sites (Ma et al., 2021). In these studies, the ATC model was used to temporally interpolate LSTs, but also to analyse the seasonal behaviour of satellite thermal observations. Additionally, the ATC parameters were used as predictors for LST downscaling.

The application of DTC models has been limited to geostationary satellites (Göttsche and Olesen, 2009) and polar orbiters with a minimum of four daily observations (Hong et al., 2018), e.g. the Moderate-Resolution Imaging Spectroradiometer (MODIS). In contrast, ATC models require many satellite observations at the same overpass time throughout the year, but allow for data gaps as long as the annual cycle is still sufficiently well represented. This permits fitting the model to low resolution data (≥1 km; Fu and Weng, 2018; Sismanidis et al., 2018) as well as to high-resolution data (≤100 m; Weng and Fu, 2014; Zhu et al., 2022). The DTC model was mainly applied for temporal interpolation and LST gap filling applications.

For applications where both seasonality and diurnal cycle play a role, a combination of ATC and DTC models is desirable. While ATC models estimate LST at one specific time of the day for the whole year, DTC models estimate LST at all times of the day for a specific day. Pérez-Planells and Göttsche (2023) presented an annual-diurnal temperature cycle (ADTC) that combines an ATC and a DTC model. By merging both,

---

[*] Corresponding author at: Mediterranean Center for Environmental Studies (CEAM), Meteorology and Climatology Area, Paterna, Spain.
[**] Corresponding author at: IMKASF, Karlsruhe Institute of Technology (KIT), Hermann-von-Helmholtz-Platz 1, 76344 Eggenstein-Leopoldshafen, Germany.
E-mail addresses: lluis@ceam.es (L. Pérez-Planells), frank.goettsche@kit.edu (F.-M. Göttsche), jan.cermak@kit.edu (J. Cermak).

https://doi.org/10.1016/j.jag.2026.105276
Received 23 November 2025; Received in revised form 30 March 2026; Accepted 2 April 2026

Table 1
Geographical and climatological information of the cities covered in the study.

City	Lat (N) / Lon (E)	Elevation (m a.s.l.)	Extension (km^2)	Annual mean temp (K) / prec. (mm)	Reference
Karlsruhe	49.0 / 8.4	118	173	283 / 800	Olonscheck and Walther (2017)
Paris	48.9 / 2.4	33	105	284 / 700	Hemmerle et al. (2019)
Madrid	40.4 / −3.7	650	607	288 / 450	Núñez-Peiró et al. (2021)
Valencia	39.5 / −3.4	16	134	291 / 500	Wei and Sobrino (2024)

the ADTC model is able to model LST at all times of the day for each day of the year, describing the annual-diurnal thermal dynamics with only five controlling parameters: fitted to MODIS data it yielded an overall RMSE of 4.2 K. The obtained parameters showed good agreement with climate regions and revealed their capability to map specific land cover features (Pérez-Planells and Göttsche, 2023). And since observation time is an independent variable of the ADTC model, arbitrarily sampled data can be fitted. This allows for the merging and joint fitting of LST products from satellites with different orbits and overpass times.

In 2018, the National Aeronautics and Space Administration (NASA) mounted the ECOsystem Spaceborne Thermal Radiometer Experiment on Space Station (ECOSTRESS) on the International Space Station (ISS). ECOSTRESS is a pilot sensor in preparation for the next generation of high-resolution TIR missions, e.g. the Indian – French space agencies cooperate on the Thermal infraRed Imaging Satellite for High-resolution Natural resource Assessment (TRISHNA) mission and the European Space Agency (ESA) Land Surface Temperature Monitoring (LSTM) mission, to be launched in 2026 and 2029, respectively. ECOSTRESS data have been used in various research fields such as evapotranspiration estimation (Cawse-Nicholson et al., 2021; Wen et al., 2022), crop monitoring (Sadri et al., 2022), urban climatology (Shreevastava et al., 2023) or post-fire analysis (Barton et al., 2023). Due to the ISS orbit, ECOSTRESS provides LST observations at a spatial resolution of 70 m with a geographical coverage between 53.6° S and 53.6° N and a variable revisit time. The latter complicates the use of ECOSTRESS in monitoring activities since its consecutive observations are acquired at different overpass times. However, ECOSTRESS offers the unique opportunity to observe the same area at different overpass times, allowing the direct modelling of the ADTC, which is impossible with data from sun-synchronous platforms, e.g., Landsat.

Here, ECOSTRESS and Landsat LSTs are merged into a multi-annual dataset and stored with their actual overpass times: these are considered in the ADTC modelling. The ADTC model was fitted to the merged dataset to obtain the annual-diurnal LST dynamics over four urban areas in Europe. The ADTC parameters obtained from the multi-annual ECOSTRESS and Landsat data were then compared with those obtained from MODIS data and analyzed by land cover. The primary

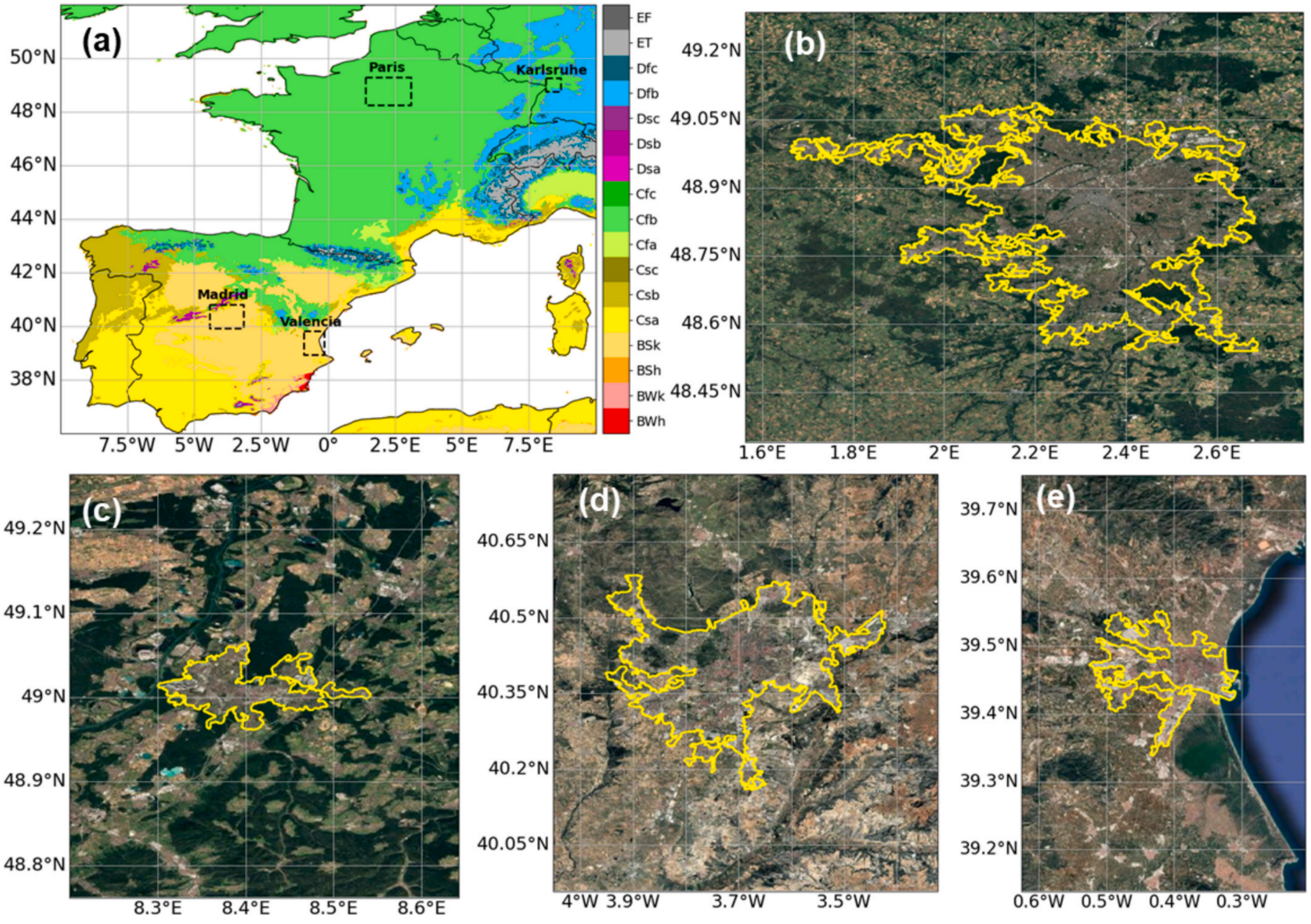

Fig. 1. Köppen-Geiger climate classes for parts of Europe (a), with the four study sites delineated by dashed line rectangles. RGB satellite view (Google Earth) for (b) Paris, (c) Karlsruhe, (d) Madrid and (e) Valencia. The yellow lines delineate the continuous urban areas according to the Corine Land Cover classification (Zhou et al., 2014). (For interpretation of the references to colour in this figure legend, the reader is referred to the web version of this article.)

objectives of this manuscript are:

- To investigate the ADTC model's performance with a merged multi-annual dataset containing high-resolution data from arbitrary overpasses.
- To evaluate the high-resolution ADTC parameters and study potential links to other surface features.

The remaining manuscript is structured as follows: Section 2 introduces the data used in this study and the analysed sites. The methodology is described in Section 3 and Section 4 assesses the performance and evaluates the ADTC parameters. The main findings and limitations of the ADTC model when applied to high-resolution data are discussed in Section 5. Finally, Section 6 summarizes these and provides the conclusions of the study.

2. Sites & data

2.1. Sites

High-resolution thermal satellite data covering four European cities were obtained: Karlsruhe (Germany), Paris (France), Madrid (Spain) and Valencia (Spain). The coordinates, elevation, extension and annual mean air temperature and precipitation for each city are given in Table 1. Fig. 1 shows the Köppen-Geiger climate classification of large parts of Europe as well as Google Earth images for each city.

2.2. High-resolution satellite data

ECOSTRESS and Landsat 8/9 LST data acquired between 2018 and 2023 were merged into a 3D-data netCDF cube needed by the ADTC model. This section describes the main features of both sensors and the used operational LST products.

2.2.1. ECOSTRESS

Due to the Earth's rotation and the inclination of the ISS's orbit, throughout the year ECOSTRESS overpass time varies with each orbit, which complicates many applications. Nevertheless, the sensor provides unprecedented high-resolution data, i.e., 70 m for Level 2 products (Hook et al., 2020), and some applications benefit from the sampling of the diurnal cycle, e.g., evapotranspiration modelling.

The ECOSTRESS LST and Emissivity (LST&E) product is used as input for the annual-diurnal temperature cycle (ADTC) model. This product uses the temperature and emissivity separation (TES; Hulley et al., 2021) algorithm to simultaneously retrieve LST&E. Hulley et al. (2021) reported a bias of −0.7 K and an RMSE of 1.1 K for 5 validation sites, while Hu et al. (2022) validated the ECOSTRESS LST&E product over 9 validation sites, with an overall bias of −0.7 K and RMSE of 2.1 K.

2.2.2. Landsat 8/9

Landsat 8 and Landsat 9 were launched in February 2013 and September 2021, respectively. The combination of both platforms, which both carry the Thermal Infrared Sensor (TIRS), provides a revisit time of 8 days. The equator crossing time of both satellites is around 10 AM on their descending orbits. TIRS data have a native spatial resolution of 100 m, which is resampled to Operational Land Imager (OLI) 30 m

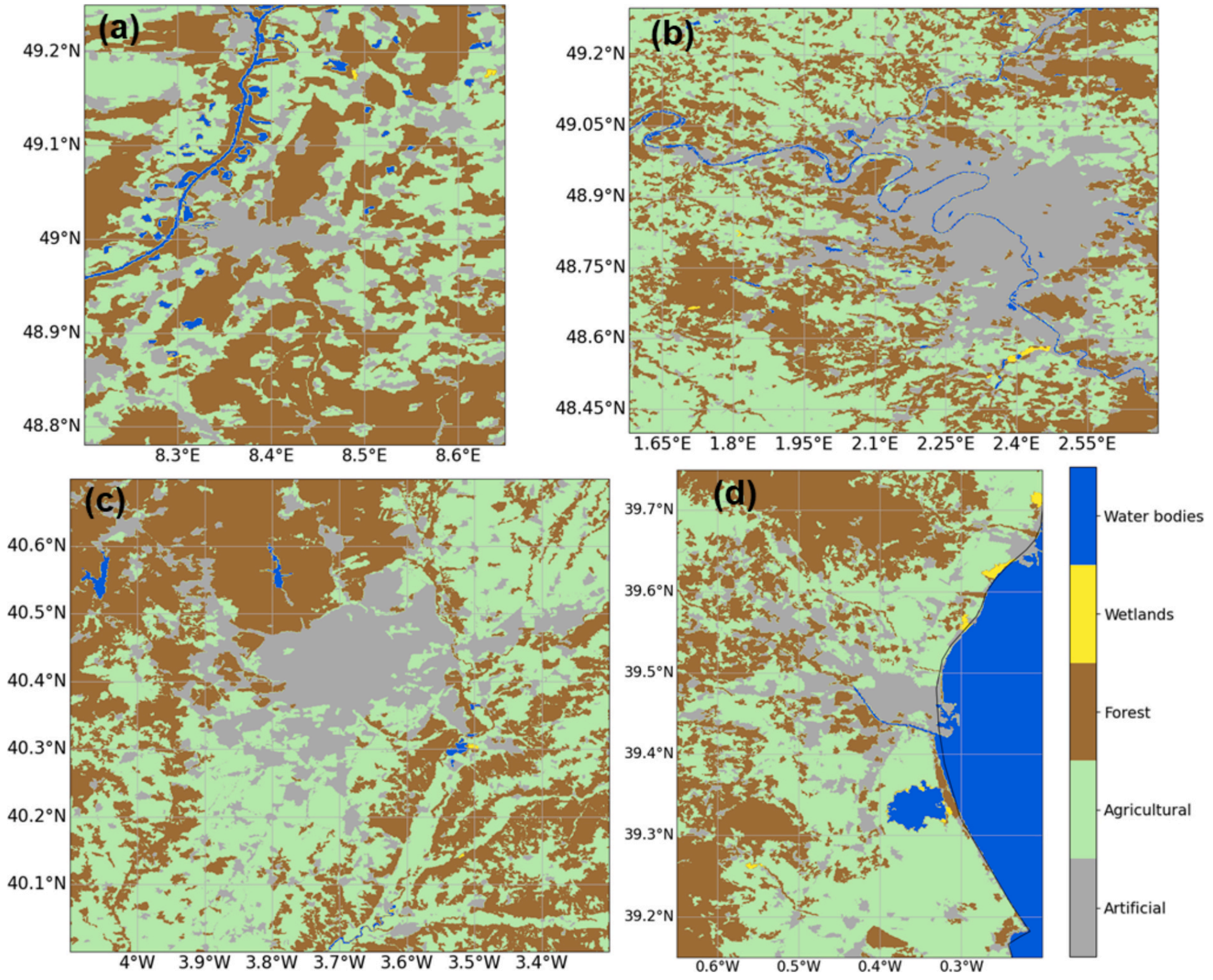

Fig. 2. CLC2018 classes for the four sites: (a) Karlsruhe, (b) Paris, (c) Madrid and (d) Valencia.

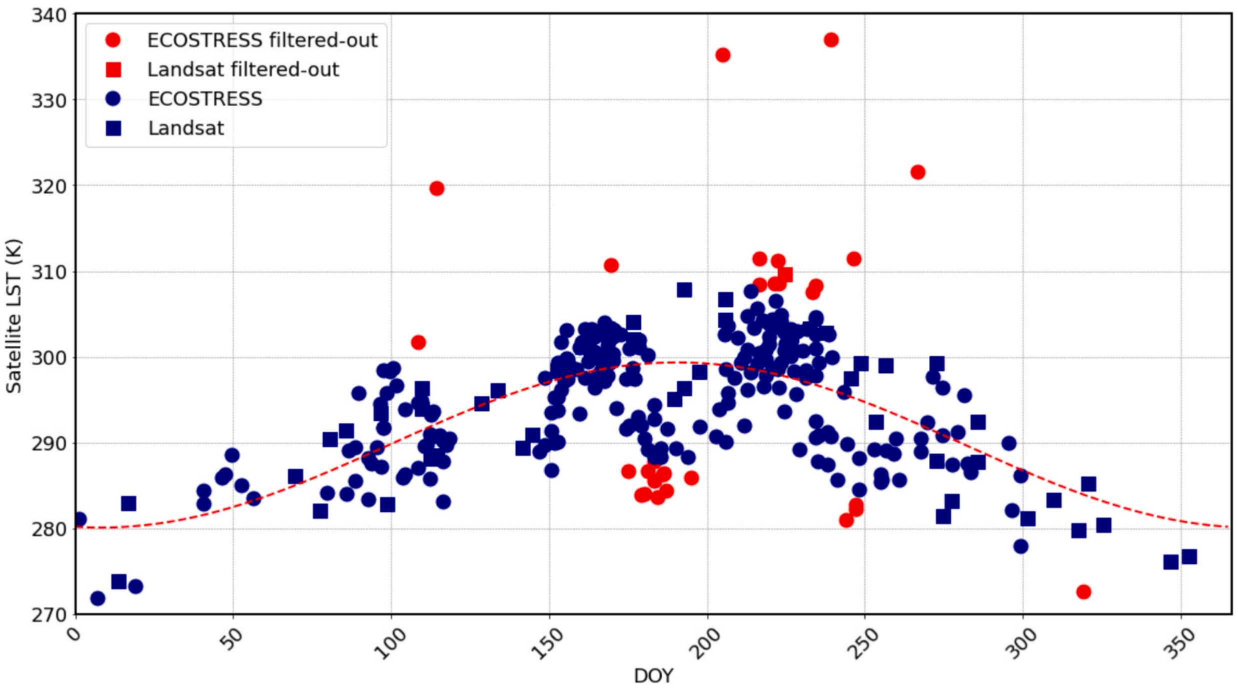

Fig. 3. Remaining data (blue symbols) after additional filtering and filtered-out data (red symbols). The dashed line represents the standard ATC fit to the time series of median LSTs (see section 3.2). The datapoints correspond to the pixel at coordinates 49.083°N, 8.430°E (forest north of Karlsruhe, Germany). (For interpretation of the references to colour in this figure legend, the reader is referred to the web version of this article.)

spatial resolution before dissemination.

The operational Landsat 8/9 LST product of the United States Geological Survey (USGS), which is retrieved with a single channel algorithm (Malakar et al., 2018), was used to complement the ECOSTRESS LST data and to increase the number of observations. The operational Landsat LST product has been validated against broadband (3 – 50 µm) and wide band (8 – 14 µm) radiometers (Guo et al., 2020; Galve et al., 2022; Hu et al., 2022) with RMSE values between 2 and 3 K, and against narrow band (9.6 – 11.5 µm) radiometers with RMSEs lower than 1.3 K (Niclòs et al., 2021, 2023; Hu et al., 2022).

2.3. *Additional data*

The parameters obtained by fitting the ADTC model to high-resolution LST data were evaluated against MODIS-derived parameters. In addition, data from the Corine Land Cover (CLC) classification were used to analyse the model parameters and to evaluate the obtained results. The following sections describe the used MODIS data and the CLC dataset.

2.3.1. *MODIS LST*

Each MODIS onboard the EOS-Aqua and EOS-Terra provides twice daily global coverage with a nominal spatial resolution of 1 km for its TIR channels, and the two satellites have equatorial crossing times of approximately 10:30 AM/PM and 1:30 AM/PM, respectively. Here, level 3 MOD11A1 and MYD11A1 LST products were used, jointly referred to as MxD11A1, which provide four daily LST observations. The MxD11A1 is delivered on a regular grid of 1 km in sinusoidal projection, and contains the weighted average by overlapping area of all MxD11 level 2 data. The MxD11 LST product was validated with an accuracy of ± 1 K (Li et al., 2021; Coll et al., 2024). All available MxD11A1 scenes from 2018 to 2023 covering the study areas were considered as reference data in the evaluation of the high-resolution ECOSTRESS-Landsat modelled data.

2.3.2. *Corine Land Cover data*

In this study, version CLC2018 of the CLC classification map produced by the European Environment Agency's Copernicus Land Monitoring Service was used. The CLC2018 product is based on Sentinel2 and Landsat 8 satellite images from 2017 and 2018 and has been validated with a global accuracy of 92 % (Moiret-Guigand, 2021). The CLC map has a spatial resolution of 250 m and contains hierarchical land covers on three different levels. Although level 3 is more detailed, only level 1 and level 2 artificial surfaces subclasses were used, which simplifies the analysis and interpretation of the maps. Fig. 1 shows the CLC2018 Level 1 classes for each study site.

3. Methodology

3.1. *ADTC model*

The ADTC model presented in Pérez-Planells and Göttsche (2023) describes the annual LST dynamics with an ATC model controlled by solar zenith angle (ATC_{sza}; Labenski, 2020) and diurnal LST variation with the DTC model GOT09 (Göttsche and Olesen, 2009). The ADTC model combines these two models and is defined as:

$$\begin{aligned} T_1(\theta) &= T_0(DOY) + T_{AD,a}\cdot\cos(\theta_z)\cdot\frac{e^{\tau(m_{min}-m(\theta_z))}}{\cos(\theta_{z,min})} && for\theta < \theta_s \\ T_2(\theta) &= T_0(DOY) + \delta T(DOY) + \left[T_{AD,a}\cdot\cos(\theta_{zs})\cdot\frac{e^{\tau(m_{min}-m(\theta_{zs}))}}{\cos(\theta_{z,min})} - \delta T\right]\cdot e^{\frac{-12h}{\pi k}(\theta-\theta_z)} && for\theta \geq \theta_s \end{aligned} \quad (1)$$

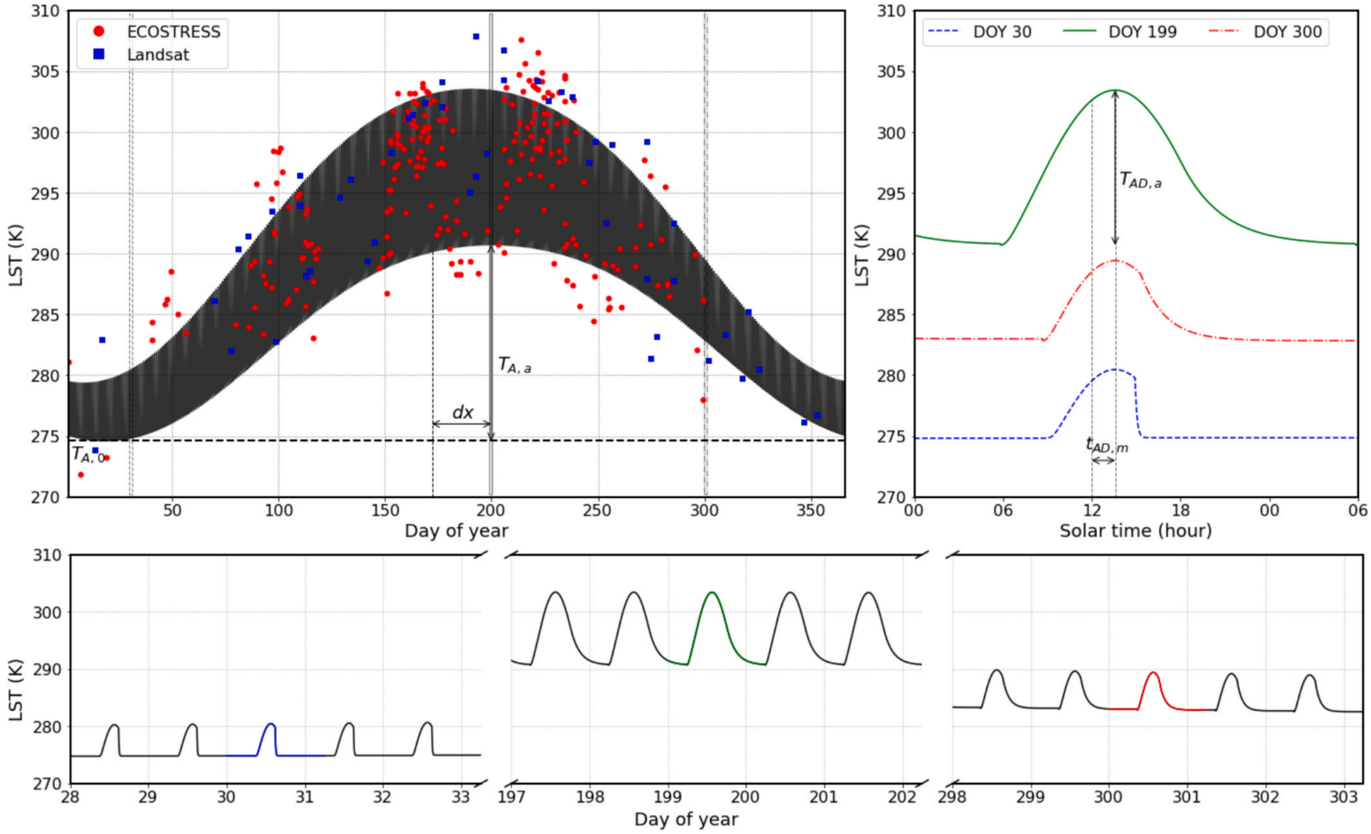

Fig. 4. LSTs obtained by fitting the ADTC model to ECOSTRESS and Landsat data for the pixel at 49.083°N, 8.430°E. The top left panel shows the satellite data and the modelled annual-diurnal variation of LST (black lines). The ADCPs controlling the annual dynamics are shown in the top-left panel. The top-right panel shows the diurnal dynamics for three selected DOY: 30, 199 and 300. The ADCPS controlling the diurnal dynamics are shown in the top-right panel. The bottom panel shows the modelled LSTs around the three selected days.

where T1 and T2 are the model temperature before and after the decay function starts at θ_s, i.e., when T2 starts. θ is the thermal hour angle with respect to thermal noon, defined as $\theta = \frac{\pi}{12h}\left(t - t_{AD,m}\right)$, with $t_{AD,m}$ as the annual mean time of maximum temperature. Thus, θ_s is the thermal hour angle at time t_s. θ_z is the solar zenith angle and $\theta_{z,min}$ its daily minimum, $m(\theta_z)$ and $m(\theta_{z,min})$ are the relative air masses at the corresponding solar zenith angles, τ is the total optical thickness and k is a constant parameter that is provided by continuity of the two functions first derivatives and ensures the smoothness between T_1 and T_2 (Göttsche and Olesen, 2009). $T_{AD,a}$ is the annual maximum daily amplitude, δT is the daily residual temperature as a function of the day of the year (DOY) and T_0 is the minimum temperature for the DOY. T_0 is estimated here with the ATC_{sza} model Labenski, 2020) to account for the annual dynamics of the temperature at sunrise, and expressed as Eq. (2):

$$\boldsymbol{T}_0(\boldsymbol{DOY}) = \boldsymbol{T}_0(\varphi, \boldsymbol{DOY}, \boldsymbol{dx}) = \boldsymbol{T}_{A,0} + \boldsymbol{T}_{A,a} \cdot \mathbf{cos}(\boldsymbol{\theta}_z(\varphi, \boldsymbol{DOY}, \boldsymbol{dx})) \tag{2}$$

where $T_{A,0}$ is the annual minimum temperature, $T_{A,a}$ is the annual amplitude of the annual minimum temperature and and θ_z depends on latitude φ, DOY and dx (lag in days) with respect to summer solstice.

After a parameter reduction performed following Hong et al. (2018), the ADTC model has five controlling parameters with physical meaning (hereafter referred to annual-diurnal cycle parameters, ADCPs): annual minimum temperature, $T_{A,0}$; annual amplitude of the annual minimum temperature, $T_{A,a}$; annual maximum daily amplitude, $T_{AD,a}$; annual mean thermal noon, $t_{AD,m}$; and lag in days with respect to summer solstice, dx. Please refer to Pérez-Planells and Göttsche (2023) for a detailed description of the ADTC model.

3.2. Data pre-processing

ECOSTRESS LST and its associated quality control band were downloaded with NASA's Appears tool (https://appeears.earthdatacloud.nasa.gov/) for the four areas defined in Section 2.1 (Fig. 1). All available data between 2018 and 2023 were downloaded and the quality control band was used to filter out low quality data, i.e. only pixels with best or nominal quality were kept in the database.

All Landsat scenes overlapping the study area and period were downloaded from the USGS Earth Explorer website (https://earthexplorer.usgs.gov/). After masking out pixels flagged as cloudy, all data were matched to the projection of ECOSTRESS using cubic resampling.

To ensure that low quality high-resolution data do not degrade the merged dataset, additional cloud filtering was applied to remove remaining outliers before fitting the model. First, all LST values below 250 K were removed (unlikely for the selected sites). Then, a moving window of 41 days was applied to estimate the median LST for the DOY at each pixel location. The resulting time series of median LST were then fitted with the standard ATC model (Bechtel, 2015). The residuals obtained with respect the fitted ATC model were then used to remove datapoints below (above) the 5th (95th) percentile. Finally, the remaining LST data for each pixel were used to fit the ADTC model. Fig. 3 shows the remaining and filtered out data when applying these additional filtering steps to a forest pixel north of Karlsruhe (Germany).

3.3. Validation strategy

All extracted MxD11A1 LST scenes were used as input for the ADTC model following Pérez-Planells and Göttsche (2023) to obtain

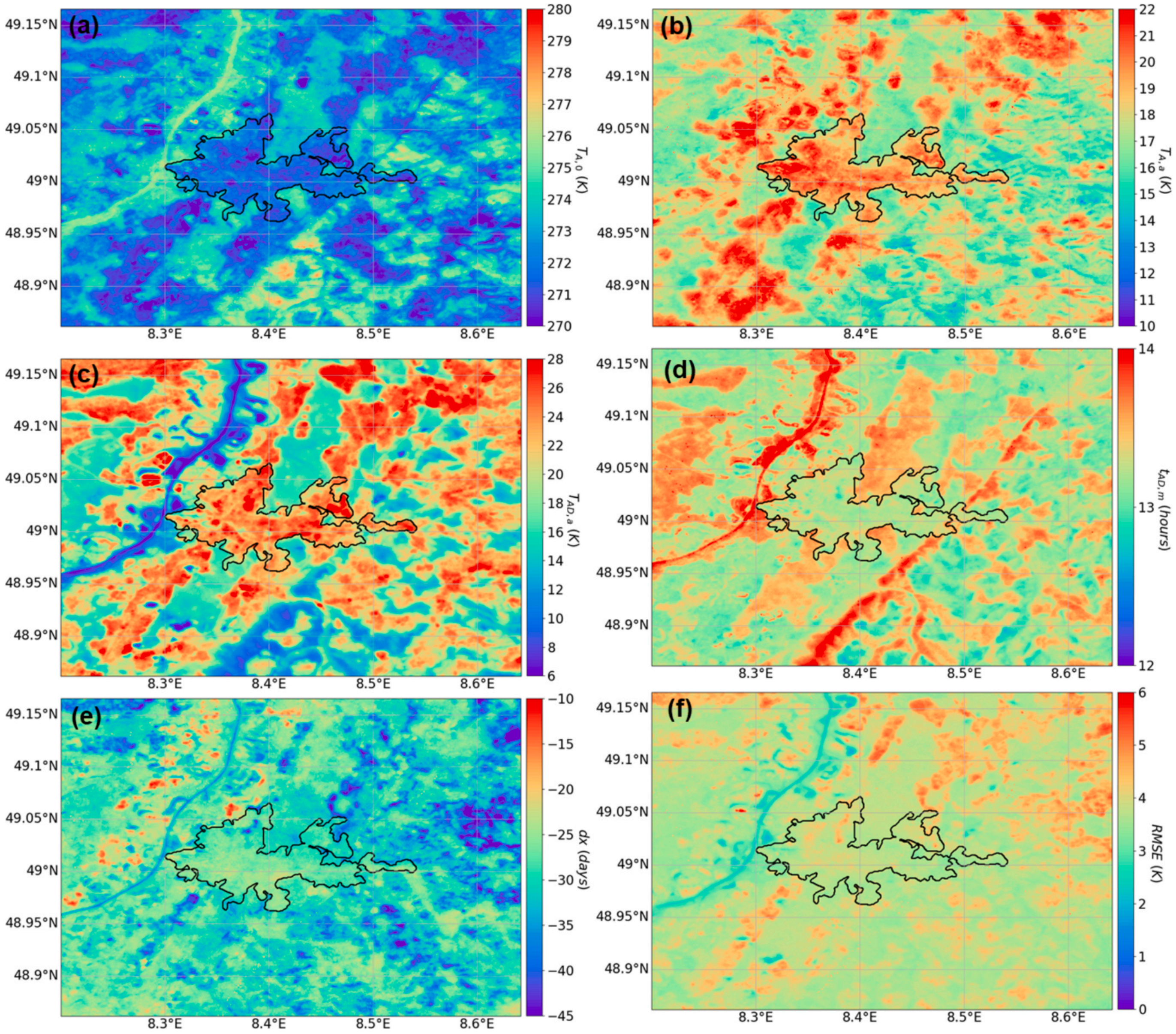

Fig. 5. High-resolution ADCPs over Karlsruhe, Germany, a) $T_{A,0}$, b) $T_{A,a}$, c) $T_{AD,a}$, d) $t_{AD,m}$, e) dx and f) RMSE of the fits. The black line delineates the urban area.

equivalent parameters to those retrieved with the high-resolution data. The ADTC derived from MODIS LSTs were validated in Pérez-Planells and Göttsche (2023) against in-situ data over three different sites, obtaining an overall RMSE of 3.4 K.

The MODIS ADCPs were used as reference for the evaluation of the high-resolution ADCPs. For a direct comparison between satellite datasets, data must be on a common grid at the spatial resolution of the coarser dataset (Pérez-Planells et al., 2023). Thus, the high-resolution ADCPs were upscaled to the spatial resolution and projection of the MODIS ADCPs. To minimize the influence of outliers on the results, the upscaled and MODIS ADCPs were compared using robust statistics (Wilrich, 2007), i.e., median of differences, robust standard deviation (RSD) and robust root mean square error (RRMSE). In addition, the CLC level 1 data were upscaled considering the majority class and resampled to MODIS projection to analyse the results by land cover.

4. Results

This section presents the results obtained by fitting the ADTC model to the merged ECOSTRESS and Landsat dataset. Fig. 4 illustrates the ADTC modelling for a single pixel: top-left panel shows the ECOSTRESS and Landsat data at coordinates 49.083°N, 8.430°E together with the simulated LSTs (black lines). The panel also illustrates the meaning of ADCPs $T_{A,0}$, $T_{A,a}$ and dx. Three (five) individual days of modelled LST are shown in the top-right (bottom) panel. The top-right panel additionally depicts the ADCPs controlling the diurnal dynamics, i.e. $T_{AD,a}$ and $t_{AD,m}$.

4.1. *High-resolution ADCPs*

This section presents the ADCPs obtained from ECOSTRESS and Landsat 8/9 data for Karlsruhe (Fig. 5), Paris (Fig. 6), Madrid (Fig. 7) and Valencia (Fig. 8). Each figure contains maps of the five ADCPs and corresponding model RMSE. The respective urban areas are delineated by black continuous lines.

For the four cities, annual minimum temperature $T_{A,0}$ had an overall mean ± standard deviation (SD) of 272.8 ± 1.7 K over CLC artificial surfaces. These are higher for the artificial surfaces near the Mediterranean Sea (Fig. 8), and slightly lower for northern latitudes (Fig. 5 and Fig. 6). At the city surroundings, $T_{A,0}$ values show a higher variability,

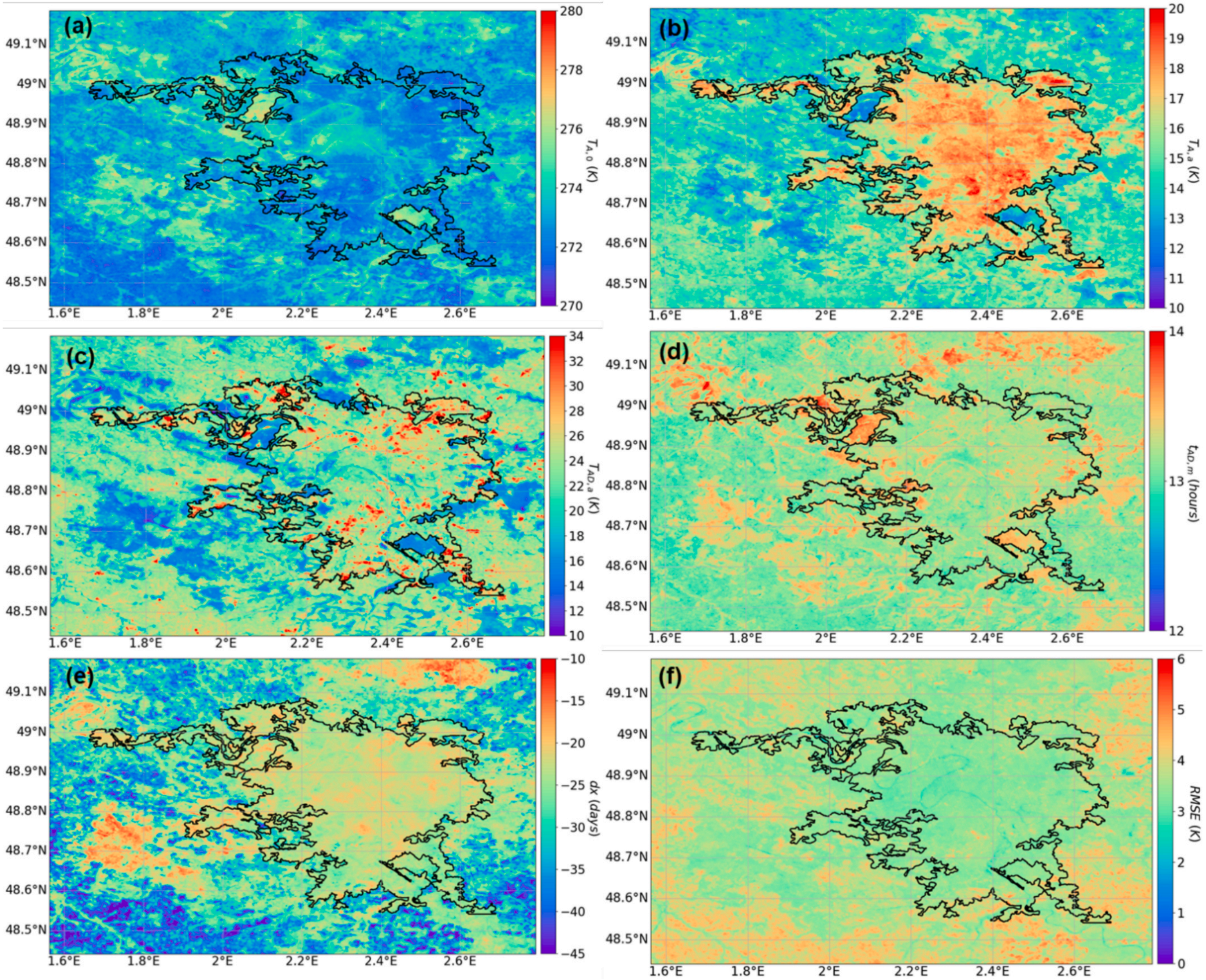

Fig. 6. High-resolution ADCPs over Paris, France, a) $T_{A,0}$, b) $T_{A,a}$, c) $T_{AD,a}$, d) $t_{AD,m}$, e) dx and f) RMSE of the fits. The black line delineates the urban area.

which depends on land cover and area. Overall, $T_{A,0}$ for agricultural areas is 272.8 ± 2.3 K, while for forest areas it is 273.7 ± 3.0 K. However, mean artificial surfaces $T_{A,0}$ for Karlsruhe and Paris are lower than corresponding forest values, while it is the opposite for Madrid and Valencia. Overall mean $T_{A,0}$ for water bodies is 282.9 ± 2.1 K. For this class, SD is larger due the wider range of values found over small lakes (values near 273 K) and the Mediterranean Sea ($T_{A,0}$ values up to 284 K). Although wetland surfaces obtained minimum temperatures closer to forests, these areas represent < 0.01 % of the analysed regions, thus their impact on the overall results is negligible.

Artificial surfaces at higher latitudes yielded lower annual temperature amplitudes $T_{A,a}$ (e.g., 19.7 ± 1.2 K for Karlsruhe) than their surroundings (17.4 ± 1.2 K for agricultural areas and 16.3 ± 1.3 K for forests). This is because vegetated areas typically have higher minimum temperatures and lower maximum temperatures in summer than sealed surfaces. However, for cities located in drier regions, e.g. Madrid, vegetation is usually less dense and crops are drier, with many bare soil fields during summer. This yields higher temperatures and, therefore, larger annual amplitudes over corresponding vegetated areas, which could lead to similar values as observed for artificial surfaces. For example, a mean $T_{A,a}$ of 20.9 K, 20.4 and 19.8 was obtained for Madrid's artificial surfaces, agricultural areas and forests, respectively. Maximum daily amplitude $T_{AD,a}$ showed similar behaviour: the vegetated surroundings of Madrid are up to 4 K higher than for the artificial surfaces, mainly due to more exposed bare soil over crop fields and sparse forests.

The time and phase shift parameters, $t_{AD,m}$ and dx, also show different patterns depending on land cover and topography. Over water bodies $t_{AD,m}$ is higher than for most land covers, e.g. it is close to 14 h at the Rhine river in Fig. 5 and Albufera lake in Fig. 8. Delayed maximum temperatures (high $t_{AD,m}$) are also observed due to topographic effects, e.g., the hills in the north-east of Madrid (Fig. 7) or the western side of the Black Forest (Fig. 5) has its daily maximum LST later than the eastern side due to the relative angle between solar azimuth angle and surface aspect. Regarding dx, cities have their maximum annual temperature closer to summer solstice, i.e. lower absolute dx (26 ± 4 days) than vegetated surfaces (generally > 30 days). An extreme case occurs over the rice paddy area south of Valencia (Fig. 8), where the absolute dx is smaller than for the city due to the rice phenology. Since vegetation starts growing in July, LSTs from then onwards are smoother than in June.

Fig. 9 shows the mean and standard deviation (SD) of the obtained ADCPs and the model RMSE for each CLC class. To compute the mean and SD over the CLC classes and to avoid mixed pixels, only pixels surrounded by the same class in a 5 x 5 pixels window were considered.

The overall RMSE of the fits is of 3.8 ± 0.7 K. The lowest RMSEs were

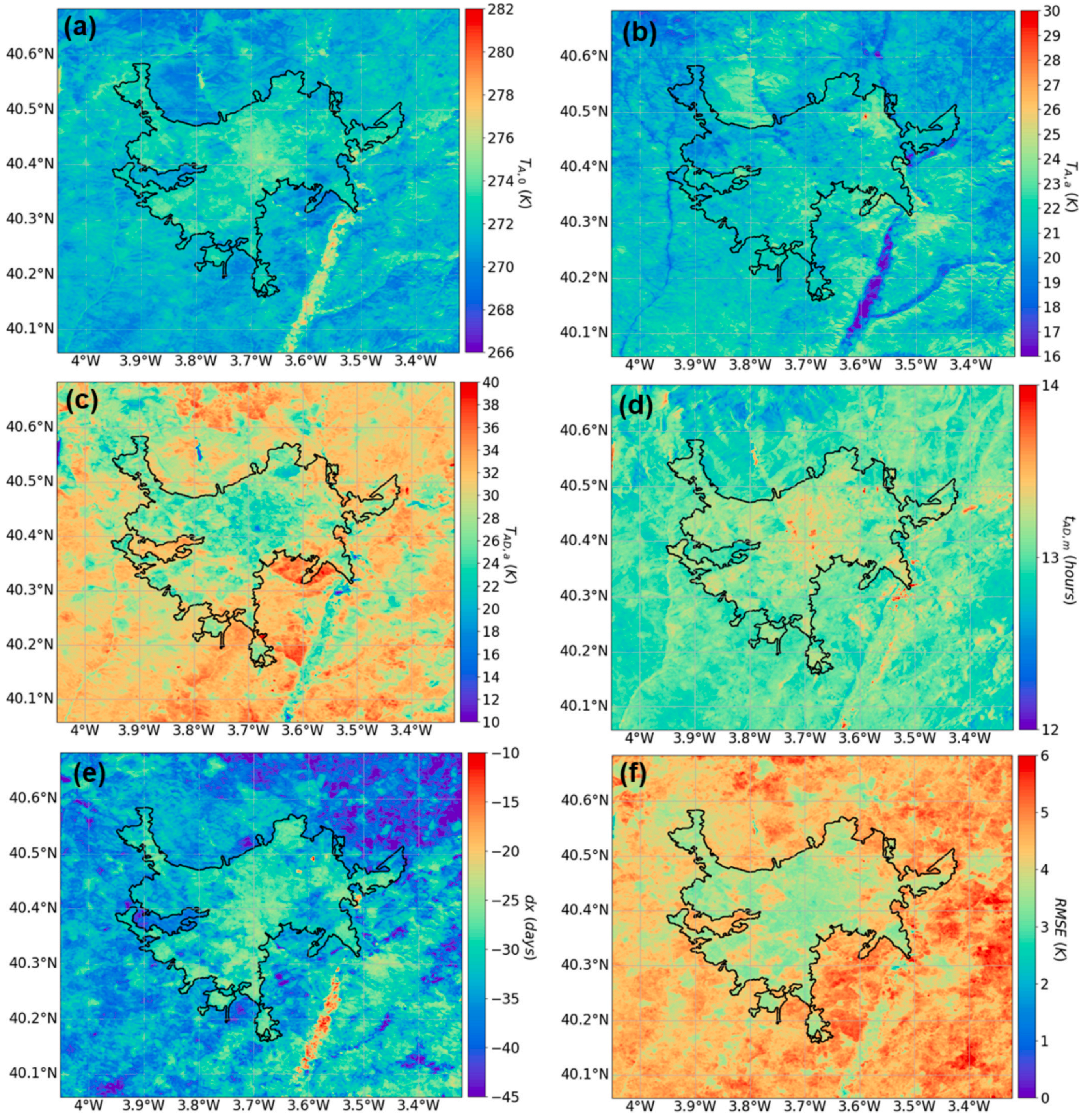

Fig. 7. High-resolution ADCPs over Madrid, Spain, a) $T_{A,0}$, b) $T_{A,a}$, c) $T_{AD,a}$, d) $t_{AD,m}$, e) dx and f) RMSE of the fits. The black line delineates the urban area.

observed over water bodies (~2 K). RMSEs of 3.5 ± 0.3 K were obtained for artificial surfaces, while they were slightly higher for vegetated areas: 3.8 ± 0.6 K over forests and 4.1 ± 0.5 K over agricultural areas, for which values up to 6 K can be found. The larger RMSEs can be partially explained by the change of land cover during harvest, which disrupts the smooth dynamics of the annual LST (e.g., rural areas around Madrid in Fig. 7).

4.2. Model evaluation

The overall statistics of the comparison between the upscaled ADCPs and the MODIS ADCPs are summarized in Table 2. Good agreement between both datasets was found for $T_{A,0}$, $T_{A,a}$, $t_{AD,m}$ and the RMSE of the fits, with RRMSE values of 1.6 K, 2.0 K, 0.2 h and 0.4 K respectively. Larger RRMSE values were found for $T_{AD,a}$ and dx (6.5 K and 6.8 days, respectively). A systematic difference was observed for $T_{AD,a}$, for which the high-resolution dataset yielded smaller amplitudes than for MODIS, maybe due to the fewer observations near maximum temperature, which also impacts the estimation of dx.

Stacked histograms of the differences between the upscaled and MODIS ADCPs at each tile are shown in Fig. 10. For $T_{A,0}$ similar performance was observed for all tiles, which indicates a good agreement between the high-resolution and the MODIS data. For Karlsruhe, Paris and Valencia, a positive median was observed, i.e. MODIS $T_{A,0}$ was

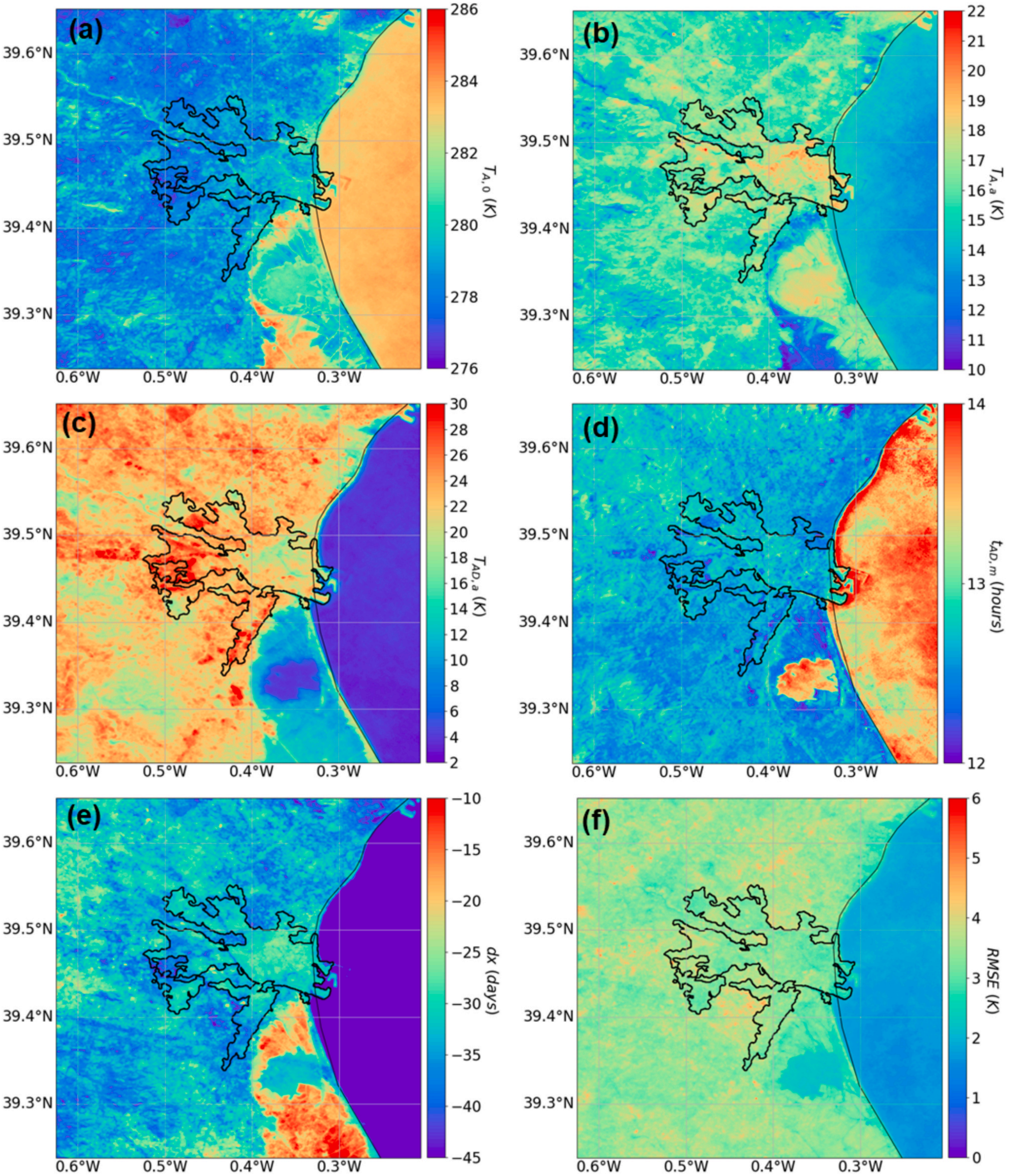

Fig. 8. High-resolution ADCPs over Valencia, Spain, a) $T_{A,0}$, b) $T_{A,a}$, c) $T_{AD,a}$, d) $t_{AD,m}$, e) dx and f) RMSE of the fits. The black line delineates the urban area.

generally lower than for the high-resolution data. This may be due to the larger number of observations near minimum temperature available from MODIS/Aqua at night-time. The RSDs for $T_{A,0}$ for each tile were between 0.5 and 1.1 K, indicating a low variability of the difference between the two datasets. The lowest RSD was obtained for Paris, which showed the narrowest distribution. The differences were also analysed considering CLC level 1 classes artificial surfaces, agricultural areas and forest areas. The analysis showed a similar performance over natural surfaces with respect to the overall data, but better median and RSD were found over artificial surfaces (0.6 K and 0.8 K, respectively). Differences in $T_{A,a}$ median values for the four tiles ranged from −0.4 K to 2.7 K and RSDs were between 0.8 and 1.8 K. The lowest median values were obtained over Paris and Karlsruhe, for which the differences approximated a normal distribution (Fig. 10b). However, over Madrid and Valencia the differences were biased and had wider distributions, especially over Madrid. The land cover analysis revealed that the larger differences for Madrid were related to agricultural land cover, which showed a median (RSD) of 3.0 K (2.1 K).

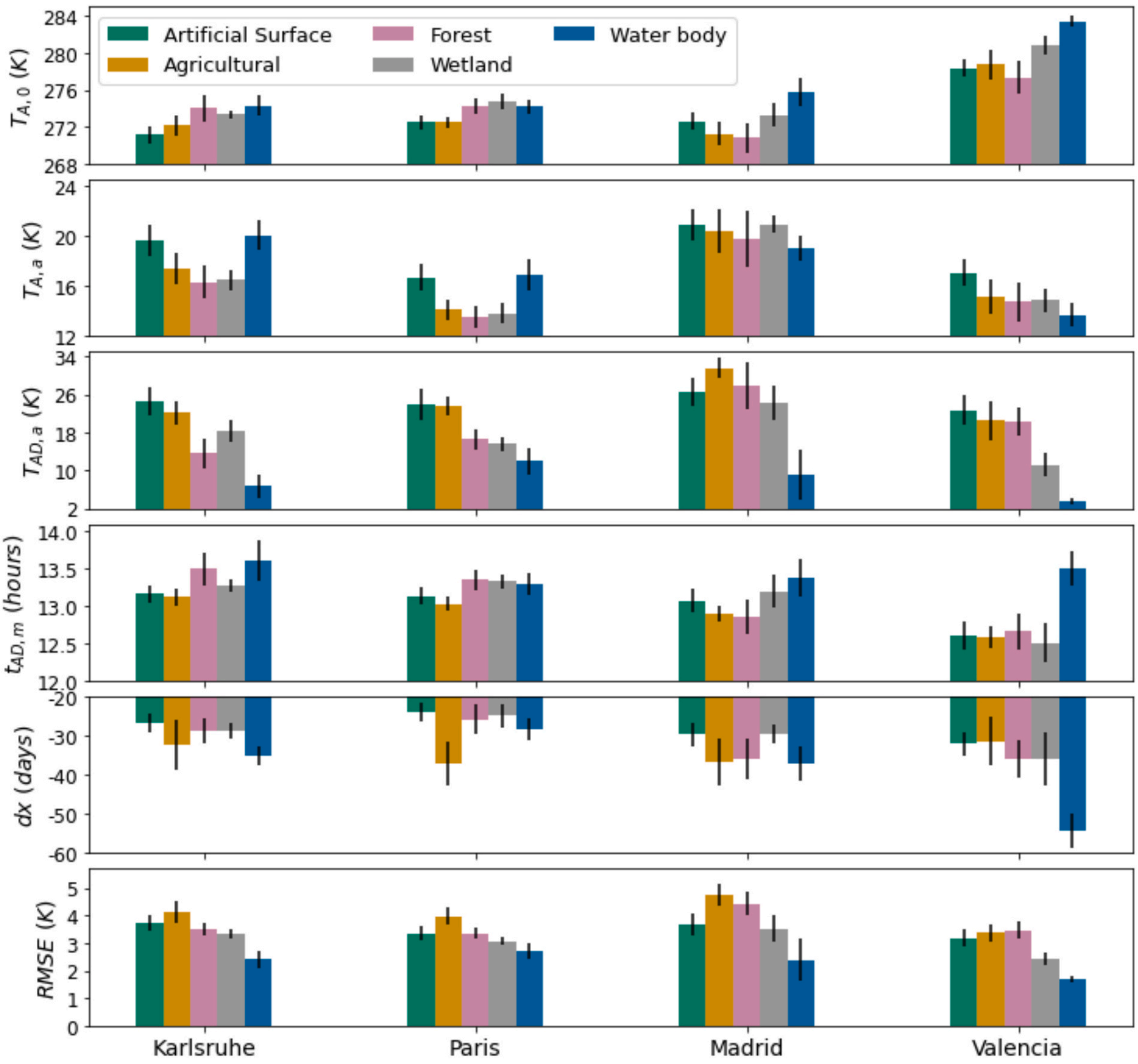

Fig. 9. Mean of the ADCPs and the model RMSE for each CLC class over the four cities. Error bars show standard deviations. Note: negative dx indicates a delay of the highest minimum annual temperature with respect to summer solstice.

Table 2
Median, RSD, RRMSE of the difference between the upscaled high-resolution ADCP and the MODIS ADCP. A total of 43,777 pixels were considered for the evaluation.

	Median	RSD	RRMSE
$T_{A,0}$ (K)	0.9	1.3	1.6
$T_{A,a}$ (K)	0.9	1.8	2.0
$T_{AD,a}$ (K)	−5.7	3.0	6.5
$t_{AD,m}$ (h)	−0.1	0.2	0.2
dx (days)	4.0	5.4	6.8
RMSE (K)	−0.3	0.4	0.4

$T_{AD,a}$ values from high-resolution data underestimated MODIS $T_{AD,a}$ for all sites and land covers, yielding negative biases, which ranged from −7.6 to −2.5 K. The systematic differences and larger RMSEs on $T_{AD,a}$ could be related to the lower number of ECOSTRESS and Landsat 8/9 observations around maximum temperature compared to MODIS, since more comparable results were obtained for $T_{A,0}$ and $T_{A,a}$. The lower number of observations near thermal noon causes an underestimation of maximum temperatures and, therefore, lowers the accuracy of $T_{AD,a}$, as well as dx. The day of the maximum annual temperature was more shifted (dx) in the high-resolution data for Karlsruhe, Paris and Valencia than for MODIS. The largest differences were observed over Paris, which showed a median (RSD) of 8.5 days (4.5 days). Madrid showed the lowest difference between both datasets, with a median (RSD) of −0.6 days (3.7 days). The RSDs for all tiles ranged between 2.5 and 2.8 days over artificial surfaces and between 3.1 and 4.4 days over natural surfaces.

A good overall agreement was observed for $t_{AD,m}$ and the RMSE of the fits. For $t_{AD,m}$, a median of −0.1 h (i.e. −6 min) was observed for Paris and Madrid, 0.1 h for Karlsruhe and −0.3 h for Valencia. RSDs were around 0.2 h for most cases. However, high-resolution RMSEs were slightly lower than for the MODIS data. Most differences ranged between −1.2 and 1.2 K, with median values between −0.6 and −0.2 K for Karlsruhe, Paris and Valencia, independent of land cover. Over Madrid, a median of −0.4 K was obtained over artificial surfaces, but slightly positive median differences (0.2 K) were found over natural surfaces, probably due to the higher RMSE observed over Madrid's surroundings (see Fig. 7f). RSDs of the comparison between RMSE values were lower than 0.4 K.

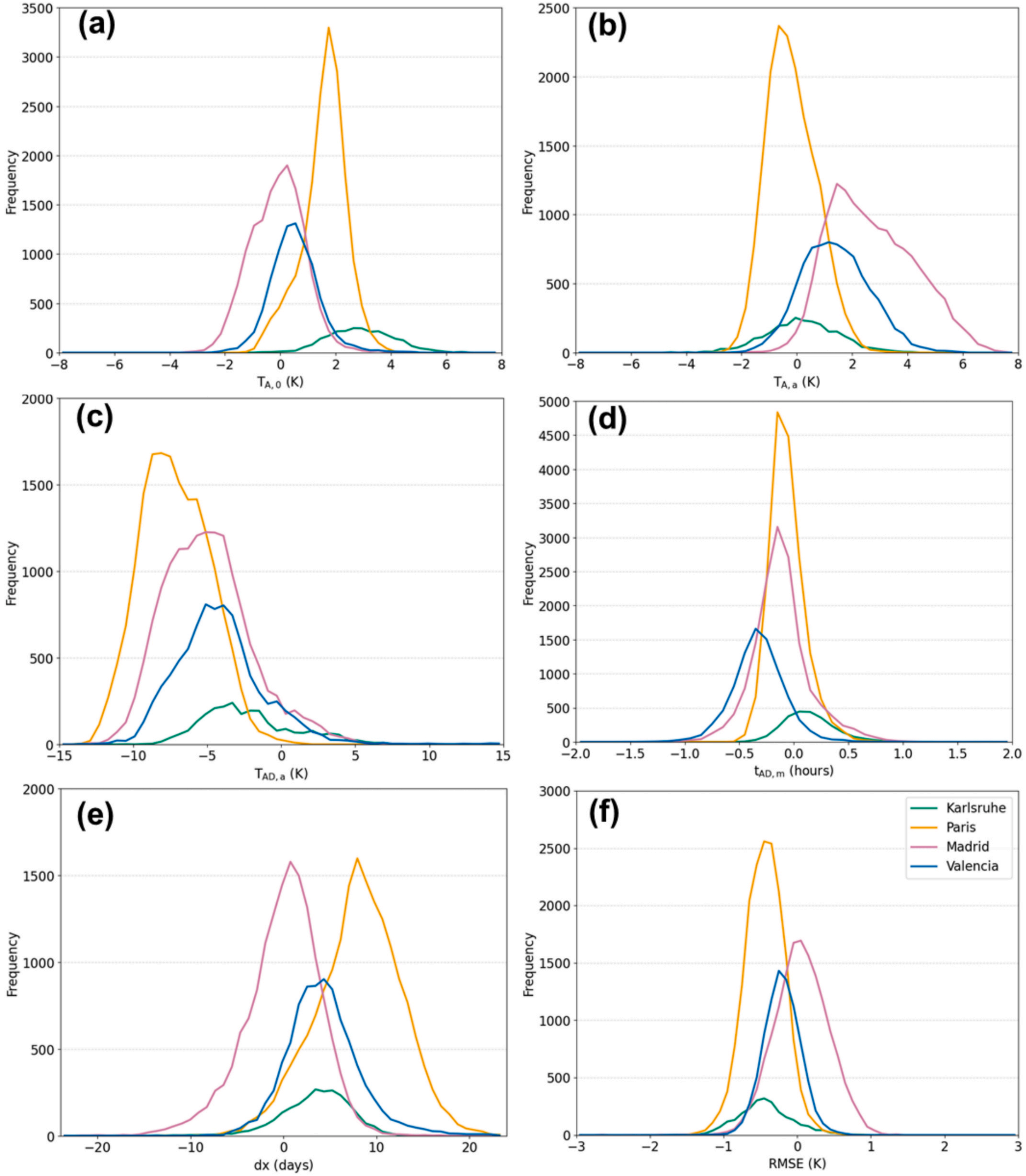

Fig. 10. Histograms of the differences between high-resolution and MODIS ADCPs: a) $T_{A,0}$, b) $T_{A,a}$, c) $T_{AD,a}$, d) $t_{AD,m}$, e) dx and f) RMSE. Colours indicate the tiles / cities.

5. Discussion

5.1. ADTC model performance

Due to the orbit of the ISS with its aleatory overpass times, ECOSTRESS provides a unique opportunity to apply the ADTC model to high-resolution data. However, due to the low temporal resolution of ECOSTRESS at mid-low latitudes as well as missing data (e.g. caused by clouds), the annual – diurnal temperature cycle is insufficiently sampled to fit the ADTC model. The mean annual number of ECOSTRESS LST

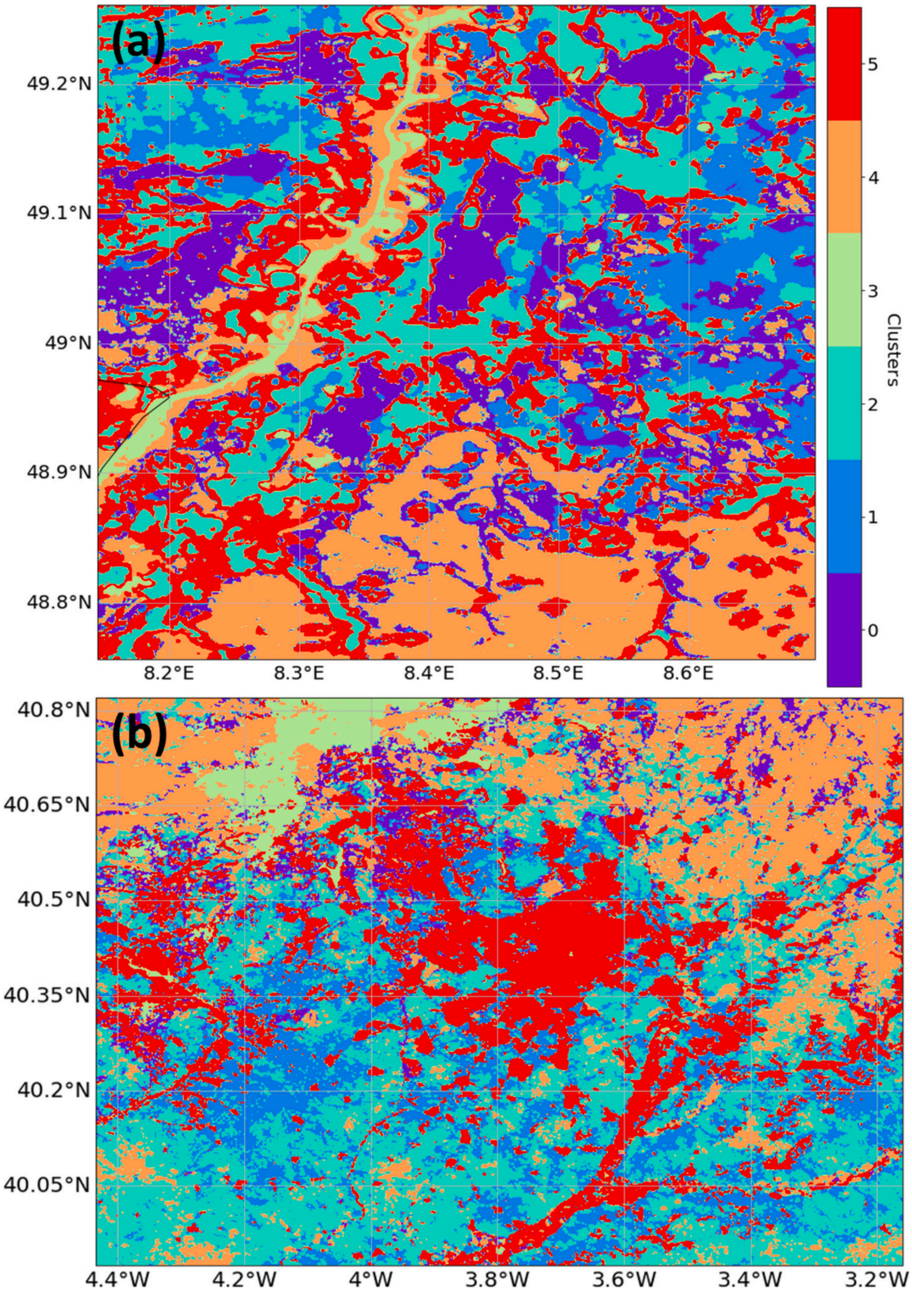

Fig. 11. K-means clusters obtained for (a) Karlsruhe and (b) Madrid considering 6 clusters.

observations per pixel and tile was 44, 54, 25 and 14 for Karlsruhe, Paris, Madrid and Valencia, respectively. Therefore, ECOSTRESS observations were complemented with LSTs from Landsat 8/9, which have a similar spatial resolution, and carefully merged into a single dataset. Additional outlier filtering avoided possible degrading of the merged dataset and improved its quality (see Section 3.2). This increased the mean annual number of observations per pixel to 58, 74, 53 and 53 for Karlsruhe, Paris, Madrid and Valencia, respectively, leading to more reliable and representative results. Since ECOSTRESS and Landsat LST products have been extensively validated in the literature and showed an accuracy that lies within ADTC model uncertainty, merging both datasets does not impact its accuracy. Possible discrepancies introduced by viewing geometry are limited by the relatively small viewing zenith angle of both sensors, which are $< 7.5^\circ$ for Landsat and $< 26^\circ$ for ECOSTRESS (Anderson et al., 2021), whereas the average effect due to the clear-sky diurnal and annual variation of solar geometry is described by the ADTC model. Furthermore, because the ADTC parameters quantify the average thermal behaviour of the observed surfaces, the effect of scale mismatch is reduced. The RMSE fit values were between 3 and 5 K, similar to those found for MODIS LSTs with the ADTC model (Pérez-Planells and Göttsche, 2023) and the ATC model (Bechtel, 2015). These results also agree with those obtained from validations against in-situ measurements for MODIS ADTC-derived LSTs (Pérez-Planells and Göttsche, 2023), which provided and overall RMSE of 3.4 K. Nevertheless, meaningful information can be extracted from larger uncertainties, which mostly relate to relatively short-term deviations from average thermal variation driven by solar geometry, e.g., harvesting periods and extreme weather situations. Previous studies account for short-term deviations from the ATC-DTC modelling when generating all-weather LST estimates (Zhan et al., 2014; Zhang et al., 2019). However, these approaches attempt to reconstruct actual satellite LST observations. Thus, additional data are needed to reduce the deviations between modelled LSTs and actual satellite LST observations, which could be achieved by integrating ATDC – modelling with machine learning and deep learning approaches.

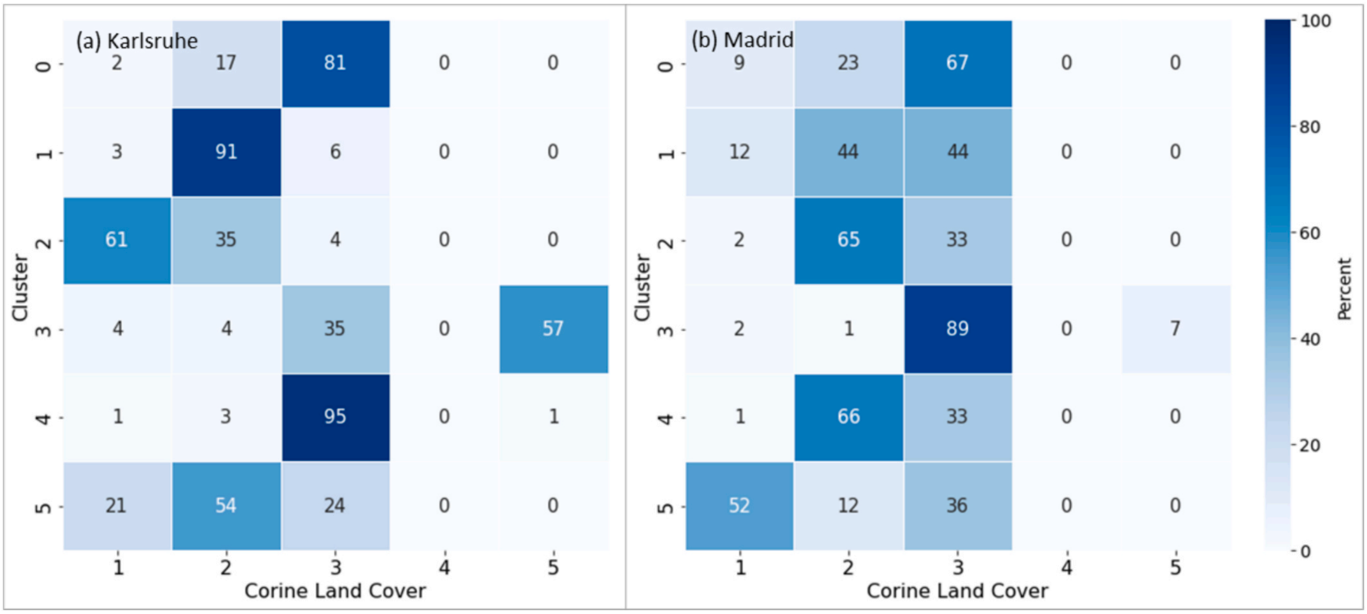

Fig. 12. Percentage of pixels corresponding to each Corine land cover class for each cluster in Fig. 11 (a) Karlsruhe and (b) Madrid. CLC level 1 classes are: 1) artificial areas, 2) agricultural areas, 3) forests, 4) wetlands, and 5) water bodies.

The ADCPs obtained for the merged high-resolution dataset were compared to those obtained for MODIS data. For both datasets the results showed good agreement for $T_{A,0}$, $T_{A,a}$, $t_{AD,m}$ and RMSE. However, larger differences were observed for $T_{AD,a}$ and dx, which are related to maximum daily and annual insolation. This is probably due to the low number of observations around noon, i.e., only 12 % of the observations are made between 11.5 and 13.5 h, which increases the uncertainty at that time and affects ADTC modelling. Since LANDSAT overpass time is around 10:30 AM, no complementary data are available around solar noon. The next high-resolution missions, e.g., TRISHNA and LSTM, will have local overpass times around 13:00 PM, which is expected to reduce uncertainty in such parameters.

5.2. *Spatial features*

5.2.1. *Land cover characterization*

Pérez-Planells and Göttsche (2023) showed that the ADCPs obtained from MODIS provided useful information regarding climatic conditions and surface properties. In this study, the higher spatial resolution allowed for more detailed investigations over smaller areas with different land covers and characteristics, e.g. rivers, lakes and urban elements such as parks.

Large water bodies, e.g. the Rhine River at Karlsruhe (Fig. 5), the Albufera Lake near Valencia (Fig. 8) or the El Pardo reservoir in Madrid (Fig. 7), can be identified. Compared to land surfaces, water body ADCPs

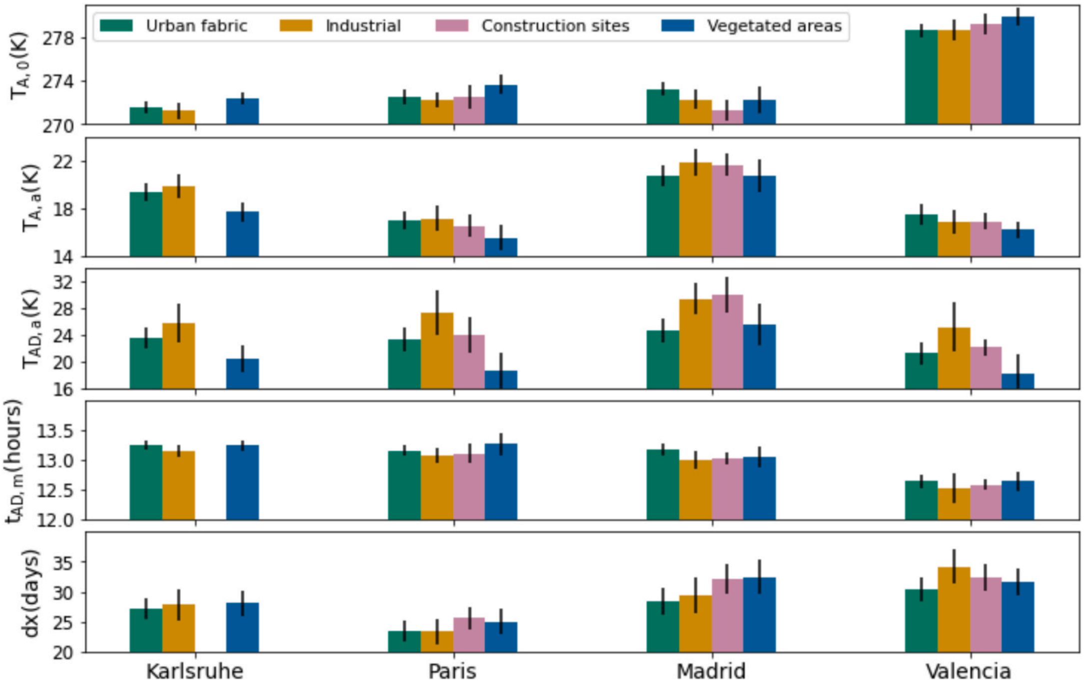

Fig. 13. Mean ADCPs for the four artificial surfaces CLC subclasses at each studied city. The error bars represent the corresponding standard deviations.

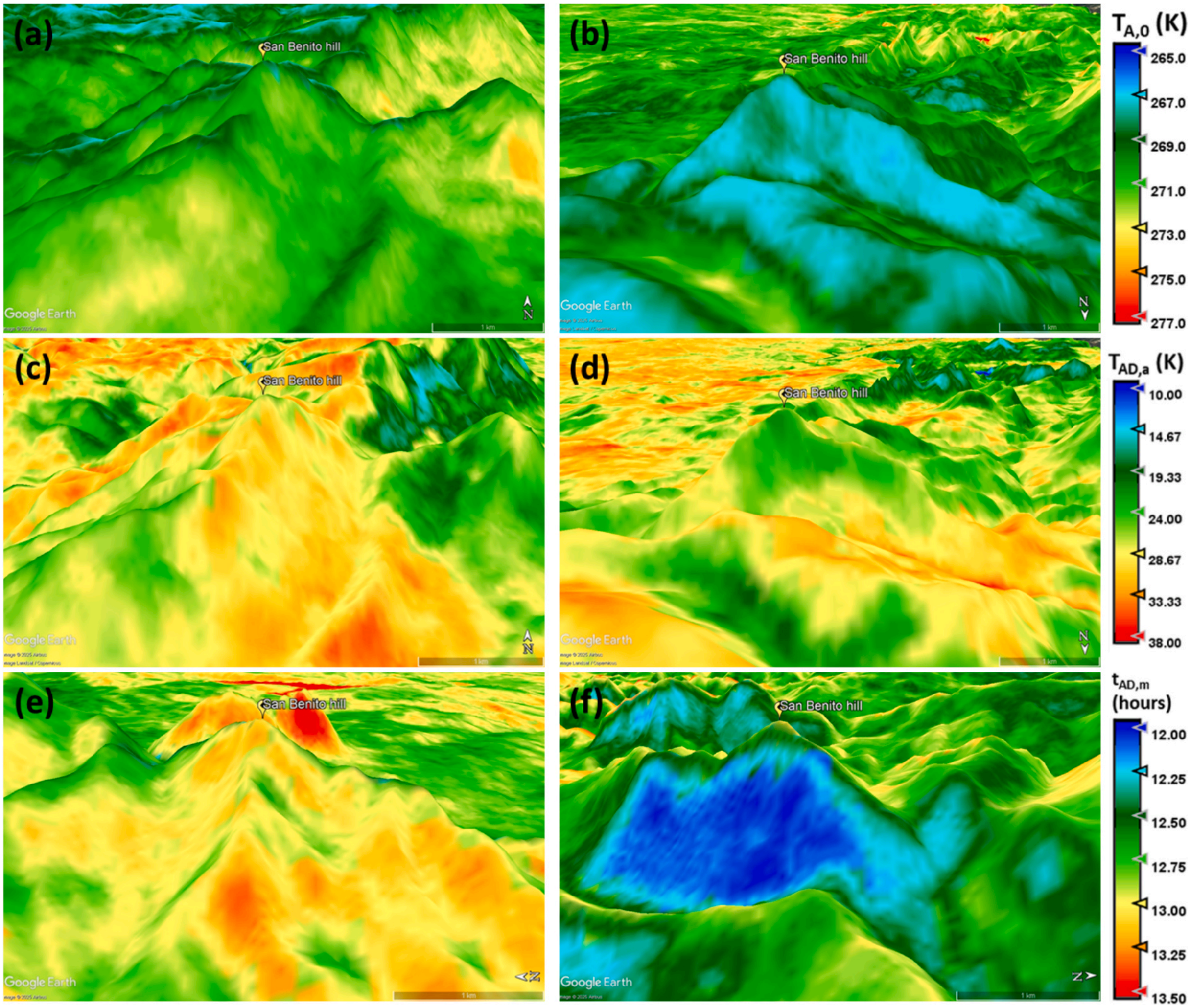

Fig. 14. $T_{A,0}$ (a,b), $T_{AD,a}$ (c, d) and $t_{AD,m}$ (e, f) of San Benito hill (Madrid, Spain, coordinates 40.555 N, −4.213 E) for different azimuthal viewing angles: (a) and (c) show the south face, (b) and (d) the north face, (e) the west face and (f) the east face.

are characterized by considerably lower $T_{AD,a}$, warmer $T_{A,0}$ and a considerable delay $t_{AD,m}$ (Pérez-Planells and Göttsche, 2023).

Around cities, the main land covers are forests and agricultural areas (Fig. 2). The surroundings of Paris and Karlsruhe, where forests are denser than around Madrid and Valencia, show higher differences between these two land covers. While forests are characterized by higher $T_{A,0}$ (above 277 K), lower amplitudes and lower $t_{AD,m}$ than cities, the corresponding values for agriculture areas are closer to those of urban areas; in contrast, their $T_{A,a}$ and $T_{A,0}$ values are lower than for urban areas and generally higher than for forests. At agriculture sites, dx depends on crop and phenology: therefore, it shows high variability. For Madrid and Valencia, the ADCP differences between forests and agricultural areas are not as distinct, mainly due to the drier and more sparse forests, which exhibit similar thermal behaviour as the agricultural surfaces. However, annual and daily amplitudes are generally larger over croplands. Over forests, $T_{A,0}$ usually shows lower values, which is mostly due to topographic effects such as elevation and surface aspect; therefore, these differences are more noticeable at higher altitudes. A k-means unsupervised classification was applied to the four tiles (scikit-learn python library, version 1.0.2) to test the separability of the different classes based on the five ADCPs and RMSE. The classification considered 6 clusters, which were later compared to the 5 Corine land cover level 1 classes. One additional cluster was allowed to represent mixed land cover pixel. Fig. 11 shows the k-means clusters obtained for Karlsruhe and Madrid, while Fig. 12 shows the corresponding percentage of pixels for each CLC class.

For Karlsruhe, most artificial surfaces are in cluster 2, representing 61 % of this cluster, while 21 % of cluster 5 pixels corresponded to artificial areas. 91 % of cluster 1 pixels correspond to agricultural pixels, but also to clusters 2 (35 %) and 5 (54 %). Forest pixels are mainly represented in clusters 0 (81 %) and 4 (95 %), but also in other clusters with mixed land covers as cluster 3 (35 %) and 5 (24 %). Water body pixels are concentrated in cluster 3 (57 %). In the case of Madrid, only cluster 3 shows a high percentage of pixels corresponding to only one CLC class, i.e., 89 % of cluster 3 pixels are associated with forest class. 52 % of cluster 5 are artificial surfaces, 65 % of clusters 2 and 4 correspond to agricultural areas and 67 % of cluster 0 are forest pixels. Cluster 1 contains a mix of artificial, agricultural and forest pixels. Although the k-means algorithm is unable to completely separate the CLC classes based on the ADCPs alone, the obtained clusters appear to be closely linked to the land covers, suggesting the usefulness of the ADCPs as land cover classification predictors. To better separate the clusters into CLC classes, additional data to the 5 ADCPs would be required. This appears to be more relevant for drier environments, where ADPCs vary over a wider range within each land cover class.

5.2.2. *Urban subclasses analysis*

Other researchers used high-resolution TIR data to investigate urban phenomena, e.g. surface urban heat island or urban hotspots, and to better understand them and their future trends (Bechtel et al., 2019;

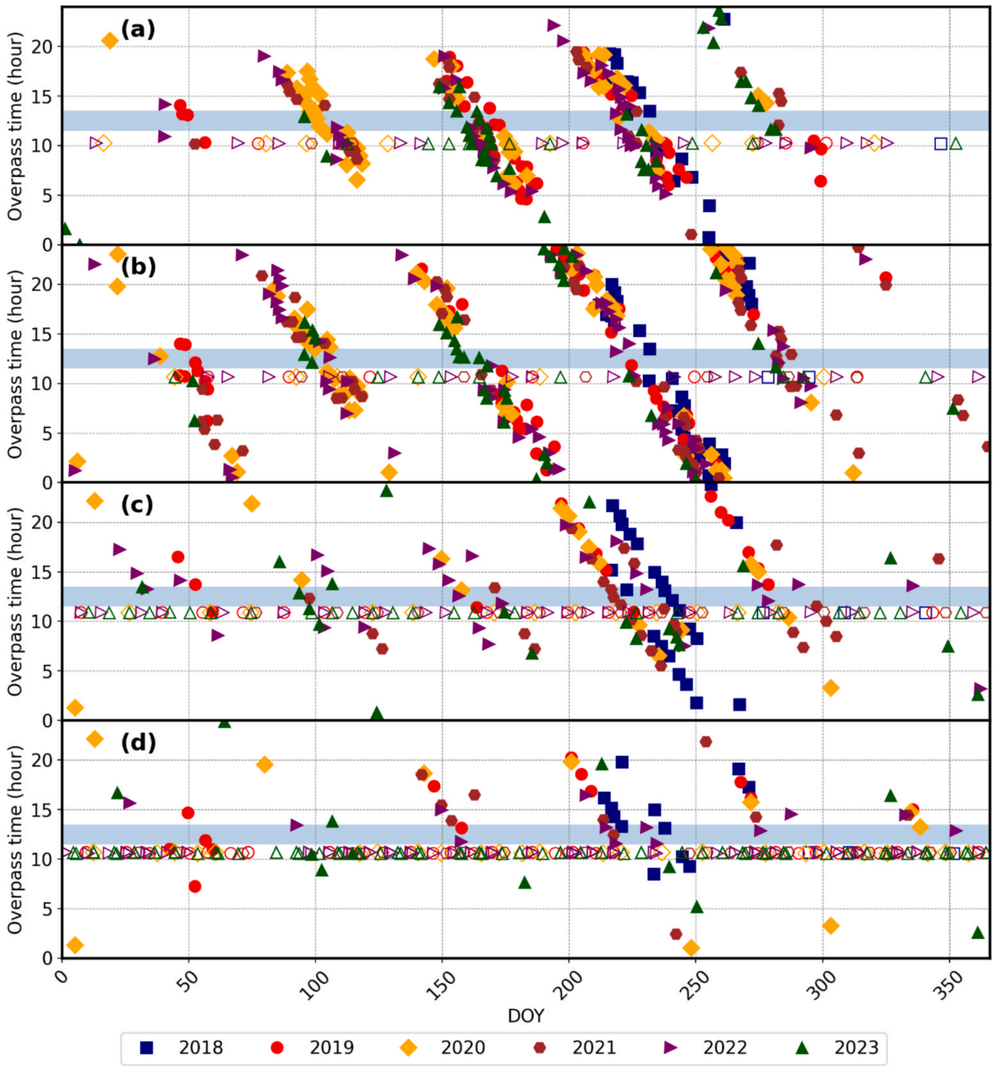

Fig. 15. ECOSTRESS (filled markers) and Landsat (unfilled markers) overpass times at each DOY for a single pixel at coordinates (a) 49.083°N, 8.430°E (north of Karlsruhe, Germany), (b) 48.870°N, 2.374°E (Paris, France), (c) 40.426°N, −3.748°E (Madrid, Spain) and (d) 39.459°N, −0.387°E (Valencia, Spain). The blue line indicates the time between 11:30 h and 13:30 h. (For interpretation of the references to colour in this figure legend, the reader is referred to the web version of this article.)

Hidalgo-García and Arco-Díaz, 2022; Wei and Sobrino, 2024). ADCPs exhibit specific patterns that could help to better understand such phenomena. To test the capability of the ADCPs to discriminate between different urban elements, they were analysed within the city boundaries delineated in Fig. 1. The ADCPs obtained for these urban areas were averaged for each of the four CLC level 2 subclasses forming the artificial surfaces class (i.e. urban fabric, industrial, construction sites and artificial vegetated areas). Fig. 13 shows the mean ADCP values and standard deviations for these four artificial surface subclasses. To compute the mean and SD over the CLC classes and to avoid mixed pixels, only pixels surrounded by the same class in a 5 x 5 pixels window were considered. For Karlsruhe, the value for construction sites is missing since this class was not encountered.

In Fig. 13, $T_{AD,a}$ shows the largest differences between classes, suggesting that $T_{AD,a}$ is the parameter that discriminates best between urban elements. Although in most cases the differences in $T_{AD,a}$ are within a standard deviation, up to 8.8 K higher values for industrial than for vegetated areas were found in Paris. Smaller differences (up to 2.1 K) were found for $T_{A,0}$ and $T_{A,a}$ over Madrid and Karlsruhe. The dx results mainly depended on the city. However, for Paris and Karlsruhe there were no significant differences between the four subclasses, but up to 4 days for Madrid and Valencia. These differences occurred between urban fabric and constructions sites in Madrid and between urban fabric and industrial areas in Valencia. Thus, significant differences between urban classes were observed for $T_{AD,a}$ and minor differences for $T_{A,0}$, $T_{A,a}$ and dx. The observed differences suggest that the ADTC model can distinguish between different urban elements and is a potential tool for analyzing urban environments.

5.2.3. *Topographic effects*

LST dynamics are mainly driven by solar geometry: therefore, topography plays a key role, especially over structured surfaces such as mountains or canyons. These landforms exhibit considerable LST anisotropy and cause the regular diurnal temperature cycle to deviate: consequently, differences in determined ADCPs are to be expected. Over mountain areas, the ADCPs depend on elevation and surface aspect. Fig. 14 shows the $T_{A,0}$, $T_{AD,a}$ and $t_{AD,m}$ values for different faces of San Benito hill near Madrid (40.55 N, −4.21 E, 1626 a.s.l.). Due to the different slopes and aspects, the $T_{A,0}$ values at the south face (a) are higher than those at the north face (b), with differences of up to 4 K. Similarly, $T_{AD,a}$ amplitudes are up to 10 K higher at the south face (c) than at the north face (d). Maximum $t_{AD,m}$ values are observed on the west face (e), since on this side insolation is highest in the afternoon, while the east face (f) receives maximum insolation in the morning or near noon, leading to earlier $t_{AD,m}$.

Fig. 14 demonstrates the capability of the ADTC model to summarize the annual-diurnal LST dynamics over complex surfaces, which reflects surface properties and structure.

5.3. Study limitations

The ADTC model has been successfully applied to six years of merged high-resolution LST data from ECOSTRESS and Landsat 8/9. The performance of the model was found to depend directly on the accuracy of the available LST data, particularly how well the LST samples represent the relevant diurnal and annual LST dynamics. ECOSTRESS data have a repeat cycle between 3 and 5 days, which can be larger over low and mid-latitudes. In addition, data gaps in TIR observations are frequent due to clouds at satellite overpass time (Anderson et al., 2021). Therefore, to increase the number of observations, six years of ECOSTRESS and Landsat data were merged into a single yearly dataset. This dataset approximates the average annual-diurnal LST dynamics over the study sites and allowed us to obtain more accurate and stable ADCPs. However, merging multi-annual data into a single yearly dataset prohibits direct studies of specific periods, e.g., at specific heatwave periods. In this sense, multi-annual parameters do not aim currently to be used for climate change or extreme weather events analysis, but large RMSE may indicate changes in land cover or land use.

Even after merging ECOSTRESS and Landsat data there are some data gaps, e.g., around noon, which increases uncertainty and leads to larger $T_{AD,a}$ and dx uncertainties compared to the MODIS ADCPs: the four daily MODIS overpasses, one of them around thermal noon, allow the sensor to capture the highest temperatures better, which yields more accurate estimates of $T_{AD,a}$ and dx. Fig. 15 shows the overpass times at each DOY for ECOSTRESS and Landsat for a single pixel centred on each site between 2018 and 2023.

These limitations, which are mainly due to insufficient data or sampling, will be reduced with the launch of several TIR high-resolution missions, which will provide daily LST data near noon. Daily data around noon and at night-time improve the representation of maximum and minimum temperatures and, consequently, the accuracy of the five ADCPs: a well-defined minimum LST improves $T_{A,0}$ and $T_{A,a}$, while better estimates of maximum LST improves $T_{AD,a}$, $t_{AD,m}$ and dx. Thus, future TIR missions are expected to enhance the accuracy of the ADTC model. Additionally, a sufficiently high sampling of LST dynamics can provide annual ADCPs instead of multi-annual ADCPs, which would be useful for monitoring applications, e.g., urban heat island studies or land cover change detection.

6. Conclusions

The ADTC model describes the smooth dynamics of LST, driven by solar geometry, with only five controlling parameters. The model was fitted to a multi-annual high-resolution LST dataset of merged ECOSTRESS and Landsat 8/9 data over four European cities with different Köppen-Geiger climate classes. The ADCPs obtained from the fits were upscaled and evaluated against corresponding MODIS ADCPs. The results showed good agreement between both datasets, especially for $T_{A,0}$, $T_{A,a}$ and $t_{AD,m}$. However, systematic differences were observed for $T_{AD,a}$ and dx, probably due to insufficient LST observations around solar noon in the high-resolution dataset. Due to the variable overpass time of ECOSTRESS, only 12 % of its observations were acquired between 11.30 h and 13:30. Future TIR high-resolution missions will have a fixed overpass time around 13:00 h and are expected to increase the accuracy of the modelling.

It is a major advantage that the ADTC model directly uses (satellite) acquisition time as an independent variable, since this allows its application to arbitrary sensors with irregular overpass times such as ECOSTRESS. The model can also be applied to data from sensors that suffer from orbital drift, such as the Advanced Very High-Resolution Radiometer (AVHRR), and to normalize LST to a nominal time.

The analysis of the ADCPs demonstrated their capability to characterize land covers based on their thermal characteristics and to capture topographic effects. While the results of the k-means classification performed on the five ADCPs alone were unsatisfactory, they suggested that the parameters contain additional information for land cover classification. In this sense, the ADCPs show considerable potential for climate change related studies, e.g., urban thermal studies and land cover change monitoring.

CRediT authorship contribution statement

Lluís Pérez-Planells: Writing – original draft, Visualization, Software, Resources, Methodology, Investigation, Formal analysis, Data curation, Conceptualization. **Frank-M. Göttsche:** Writing – review & editing, Validation, Supervision, Resources, Methodology, Conceptualization. **Jan Cermak:** Writing – review & editing, Validation, Supervision.

Declaration of competing interest

The authors declare that they have no known competing financial interests or personal relationships that could have appeared to influence the work reported in this paper.

Acknowledgements

The authors would like to acknowledge the North American Space Agency (NASA) and the U.S. Geological Survey for providing the ECOSTRESS and Landsat LST products used in this study.

Data availability

Data will be made available on request.

References

Anderson, M.C., Yang, Y., Xue, J., Knipper, K.R., Yang, Y., Gao, F., Hain, C.R., Kustas, W. P., Cawse-Nicholson, K., Hulley, G., Fisher, J.B., Alfieri, J.G., Meyers, T.P., Prueger, J., Baldocchi, D.D., Rey-Sanchez, C., 2021. Interoperability of ECOSTRESS and Landsat for mapping evapotranspiration time series at sub-field scales. Remote Sens. Environ. 252, 112189. https://doi.org/10.1016/j.rse.2020.112189.

Barton, A.M., Poulos, H.M., Koch, G.W., Kolb, T.E., Thode, A.E., 2023. Detecting patterns of post-fire pine regeneration in a Madrean Sky Island with field surveys and remote sensing. Sci. Total Environ. 867, 161517. https://doi.org/10.1016/j.scitotenv.2023.161517.

Bechtel, B., 2015. A new global climatology of annual land surface temperature. Remote Sens. (Basel) 7, 2850–2870. https://doi.org/10.3390/rs70302850.

Bechtel, B., Demuzere, M., Mills, G., Zhan, W., Sismanidis, P., Small, C., Voogt, J., 2019. SUHI analysis using local climate Zones—A comparison of 50 cities. Urban Clim. 28, 100451. https://doi.org/10.1016/j.uclim.2019.01.005.

Cawse-Nicholson, K., Anderson, M.C., Yang, Y., Yang, Y., Hook, S.J., Fisher, J.B., Halverson, G., Hulley, G.C., Hain, C., Baldocchi, D.D., Brunsell, N.A., Desai, A.R., Griffis, T.J., Novick, K.A., 2021. Evaluation of a CONUS-Wide ECOSTRESS DisALEXI evapotranspiration product. IEEE J. Sel. Top. Appl. Earth Obs. Remote Sens. 14, 10117–10133. https://doi.org/10.1109/JSTARS.2021.3111867.

Coll, C., Niclòs, R., Puchades, J., García-Santos, V., Perelló, M., Pérez-Planells, L., 2024. Demonstrating the suitability of the radiance- based method for assessing the accuracy of MODIS land surface temperature products. IEEE Trans. Geosci. Remote Sens. 62, 1–15. https://doi.org/10.1109/TGRS.2024.3454377.

Fu, P., Weng, Q., 2018. Variability in annual temperature cycle in the urban areas of the United States as revealed by MODIS imagery. ISPRS J. Photogramm. Remote Sens. 146, 65–73. https://doi.org/10.1016/j.isprsjprs.2018.09.003.

Galve, J.M., Sánchez, J.M., García-Santos, V., González-Piqueras, J., Calera, A., Villodre, J., 2022. Assessment of land surface temperature estimates from Landsat 8-TIRS in a high-contrast semiarid agroecosystem. Algorithms Intercomparison. Remote Sens. (Basel). 14, 1843. https://doi.org/10.3390/rs14081843.

Göttsche, F.M., Olesen, F.S., 2009. Modelling the effect of optical thickness on diurnal cycles of land surface temperature. Remote Sens. Environ. 113, 2306–2316. https://doi.org/10.1016/j.rse.2009.06.006.

Guo, J., Ren, H., Zheng, Y., Lu, S., Dong, J., 2020. Evaluation of land surface temperature retrieval from landsat 8/TIRS images before and after stray light correction using the SURFRAD dataset. Remote Sens. (Basel). 12. https://doi.org/10.3390/rs12061023.

Hemmerle, H., Hale, S., Dressel, I., Benz, S.A., Attard, G., Blum, P., Bayer, P., 2019. Estimation of groundwater temperatures in Paris, France. Geofluids 2019, 1–11. https://doi.org/10.1155/2019/5246307.

Hidalgo-García, D., Arco-Díaz, J., 2022. Modeling the Surface Urban Heat Island (SUHI) to study of its relationship with variations in the thermal field and with the indices of land use in the metropolitan area of Granada (Spain). Sustain. Cities Soc. 87, 104166. https://doi.org/10.1016/j.scs.2022.104166.

Hong, F., Zhan, W., Göttsche, F.M., Liu, Z., Zhou, J., Huang, F., Lai, J., Li, M., 2018. Comprehensive assessment of four-parameter diurnal land surface temperature cycle models under clear-sky. ISPRS J. Photogramm. Remote Sens. 142, 190–204. https://doi.org/10.1016/j.isprsjprs.2018.06.008.

Hook, S.J., Cawse-Nicholson, K., Barsi, J., Radocinski, R., Hulley, G.C., Johnson, W.R., Rivera, G., Markham, B., 2020. In-flight validation of the ECOSTRESS, Landsats 7 and 8 thermal infrared spectral channels using the lake tahoe CA/NV and Salton Sea CA automated validation sites. IEEE Trans. Geosci. Remote Sens. 58, 1294–1302. https://doi.org/10.1109/TGRS.2019.2945701.

Hu, T., Mallick, K., Hulley, G.C., Planells, L.P., Göttsche, F.M., Schlerf, M., Hitzelberger, P., Didry, Y., Szantoi, Z., Alonso, I., Sobrino, J.A., Skoković, D., Roujean, J.-L., Boulet, G., Gamet, P., Hook, S., 2022. Continental-scale evaluation of three ECOSTRESS land surface temperature products over Europe and Africa: Temperature-based validation and cross-satellite comparison. Remote Sens. Environ. 282, 113296. https://doi.org/10.1016/j.rse.2022.113296.

Hulley, G.C., Gottsche, F.M., Rivera, G., Hook, S.J., Freepartner, R.J., Martin, M.A., Cawse-Nicholson, K., Johnson, W.R., 2021. Validation and quality assessment of the ECOSTRESS level-2 land surface temperature and emissivity product. IEEE Trans. Geosci. Remote Sens. 1–23. https://doi.org/10.1109/TGRS.2021.3079879.

Labenski, P., 2020. Detection of Geothermal Anomalies with Annual Cycle Parameters (ACP). Karlsruhe Institute of Technology, Karlsruhe, Germany.

Li, H., Li, R., Yang, Y., Cao, B., Bian, Z., Hu, T., Du, Y., Sun, L., Liu, Q., 2021. Temperature-based and radiance-based validation of the collection 6 MYD11 and MYD21 land surface temperature products over barren surfaces in Northwestern China. IEEE Trans. Geosci. Remote Sens. 59, 1794–1807. https://doi.org/10.1109/TGRS.2020.2998945.

Liu, X., Tang, B.-H., Li, Z.-L., Zhou, C., Wu, W., Rasmussen, M.O., 2020. An improved method for separating soil and vegetation component temperatures based on diurnal temperature cycle model and spatial correlation. Remote Sens. Environ. 248, 111979. https://doi.org/10.1016/j.rse.2020.111979.

Ma, J., Zhou, J., Göttsche, F.-M., Liang, S., Wang, S., Li, M., 2020. A global long-term (1981–2000) land surface temperature product for NOAA AVHRR. Earth Syst. Sci. Data 12, 3247–3268. https://doi.org/10.5194/essd-12-3247-2020.

Ma, J., Zhou, J., Liu, S., Göttsche, F.M., Zhang, X., Wang, S., Li, M., 2021. Continuous evaluation of the spatial representativeness of land surface temperature validation sites. Remote Sens. Environ. 265. https://doi.org/10.1016/j.rse.2021.112669.

Malakar, N.K., Hulley, G.C., Hook, S.J., Laraby, K., Cook, M., Schott, J.R., 2018. An operational land surface temperature product for landsat thermal data: methodology and validation. IEEE Trans. Geosci. Remote Sens. 56, 5717–5735. https://doi.org/10.1109/TGRS.2018.2824828.

Moiret-Guigand, A., 2021. Corine land cover 2018 validation report. CLMS Land Product Validation.

Niclòs, R., Perelló, M., Puchades, J., Coll, C., Valor, E., 2023. Evaluating Landsat-9 TIRS-2 calibrations and land surface temperature retrievals against ground measurements using multi-instrument spatial and temporal sampling along transects. Int. J. Appl. Earth Obs. Geoinf. 125, 103576. https://doi.org/10.1016/j.jag.2023.103576.

Niclòs, R., Puchades, J., Coll, C., Barberà, M.J., Pérez-Planells, L., Valiente, J.A., Sánchez, J.M., 2021. Evaluation of Landsat-8 TIRS data recalibrations and land surface temperature split-window algorithms over a homogeneous crop area with different phenological land covers. ISPRS J. Photogramm. Remote Sens. 174, 237–253. https://doi.org/10.1016/j.isprsjprs.2021.02.005.

Núñez-Peiró, M., Sánchez-Guevara Sánchez, C., Neila González, F.J., 2021. Hourly evolution of intra-urban temperature variability across the local climate zones. The Case of Madrid. Urban Clim. 39, 100921. https://doi.org/10.1016/j.uclim.2021.100921.

Olonscheck, M., Walther, C., 2017. Methods to assess heat exposure: a comparison of fine-scale approaches within the German city of Karlsruhe. Urban Clim. 19, 41–53. https://doi.org/10.1016/j.uclim.2016.12.001.

Pérez-Planells, L., Ghent, D., Ermida, S., Martin, M., Göttsche, F.-M., 2023. Retrieval consistency between LST CCI satellite data products over Europe and Africa. Remote Sens. (Basel). 15, 3281. https://doi.org/10.3390/rs15133281.

Pérez-Planells, L., Göttsche, F.-M., 2023. Combined modelling of annual and diurnal land surface temperature cycles. Remote Sens. Environ. 299, 113892. https://doi.org/10.1016/j.rse.2023.113892.

Sadri, S., Famiglietti, J.S., Pan, M., Beck, H.E., Berg, A., Wood, E.F., 2022. FarmCan: a physical, statistical, and machine learning model to forecast crop water deficit for farms. Hydrol. Earth Syst. Sci. 26, 5373–5390. https://doi.org/10.5194/hess-26-5373-2022.

Shreevastava, A., Raymond, C., Hulley, G.C., 2023. Contrasting intraurban signatures of humid and dry heatwaves over Southern California. J. Appl. Meteorol. Climatol. 62, 709–720. https://doi.org/10.1175/JAMC-D-22-0149.1.

Sismanidis, P., Bechtel, B., Keramitsoglou, I., Kiranoudis, C.T., 2018. Mapping the Spatiotemporal Dynamics of Europe's Land Surface Temperatures. IEEE Geosci. Remote Sens. Lett. 15, 202–206. https://doi.org/10.1109/LGRS.2017.2779829.

Sismanidis, P., Keramitsoglou, I., Bechtel, B., Kiranoudis, C.T., 2017. Improving the downscaling of diurnal land surface temperatures using the annual cycle parameters as disaggregation kernels. Remote Sens. (Basel) 9. https://doi.org/10.3390/rs9010023.

Wei, L., Sobrino, J.A., 2024. Surface urban heat island analysis based on local climate zones using ECOSTRESS and Landsat data: a case study of Valencia city (Spain). Int. J. Appl. Earth Obs. Geoinf. 130, 103875. https://doi.org/10.1016/j.jag.2024.103875.

Wen, J., Fisher, J.B., Parazoo, N.C., Hu, L., Litvak, M.E., Sun, Y., 2022. Resolve the clear-sky continuous diurnal cycle of high-resolution ECOSTRESS evapotranspiration and land surface temperature. Water Resour. Res. 58. https://doi.org/10.1029/2022WR032227.

Weng, Q., Fu, P., 2014. Modeling annual parameters of clear-sky land surface temperature variations and evaluating the impact of cloud cover using time series of Landsat TIR data. Remote Sens. Environ. 140, 267–278. https://doi.org/10.1016/j.rse.2013.09.002.

Wilrich, P.T., 2007. Robust estimates of the theoretical standard deviation to be used in interlaboratory precision experiments. Accred. Qual. Assur. 12, 231–240. https://doi.org/10.1007/s00769-006-0240-7.

Yang, Y., Zhao, W., Yang, Y., Xu, M., Mukhtar, H., Tauqir, G., Tarolli, P., 2024. An annual temperature cycle feature constrained method for generating MODIS daytime all-weather land surface temperature. IEEE Trans. Geosci. Remote Sens. 62, 1–14. https://doi.org/10.1109/TGRS.2024.3377670.

Zhan, W., Zhou, J., Ju, W., Li, M., Sandholt, I., Voogt, J., Yu, C., 2014. Remotely sensed soil temperatures beneath snow-free skin-surface using thermal observations from tandem polar-orbiting satellites: an analytical three-time-scale model. Remote Sens. Environ. 143, 1–14. https://doi.org/10.1016/j.rse.2013.12.004.

Zhang, X., Zhou, J., Gottsche, F.-M., Zhan, W., Liu, S., Cao, R., 2019. A method based on temporal component decomposition for estimating 1-km all-weather land surface temperature by merging satellite thermal infrared and passive microwave observations. IEEE Trans. Geosci. Remote Sens. 57, 4670–4691. https://doi.org/10.1109/TGRS.2019.2892417.

Zhou, D., Zhao, S., Liu, S., Zhang, L., Zhu, C., 2014. Surface urban heat island in China's 32 major cities: spatial patterns and drivers. Remote Sens. Environ. 152, 51–61. https://doi.org/10.1016/j.rse.2014.05.017.

Zhu, X., Duan, S.-B., Li, Z.-L., Wu, P., Wu, H., Zhao, W., Qian, Y., 2022. Reconstruction of land surface temperature under cloudy conditions from Landsat 8 data using annual temperature cycle model. Remote Sens. Environ. 281, 113261. https://doi.org/10.1016/j.rse.2022.113261.